PROTEINS
STRUCTURE ■ FUNCTION ■ BIOINFORMATICS

Multiscale modeling of structural dynamics underlying force generation and product release in actomyosin complex

Wenjun Zheng*

Physics Department, University at Buffalo, Buffalo, New York 14260

ABSTRACT

To decrypt the mechanistic basis of myosin motor function, it is essential to probe the conformational changes in actomyosin with high spatial and temporal resolutions. In a computational effort to meet this challenge, we have performed a multiscale modeling of the allosteric couplings and transition pathway of actomyosin complex by combining coarse-grained modeling of the entire complex with all-atom molecular dynamics simulations of the active site. Our modeling of allosteric couplings at the pre-powerstroke state has pinpointed key actin-activated couplings to distant myosin parts which are critical to force generation and the sequential release of phosphate and ADP. At the post-powerstroke state, we have identified isoform-dependent couplings which underlie the reciprocal coupling between actin binding and nucleotide binding in fast Myosin II, and load-dependent ADP release in Myosin V. Our modeling of transition pathway during powerstroke has outlined a clear sequence of structural events triggered by actin binding, which lead to subsequent force generation, twisting of central β-sheet, and the sequential release of phosphate and ADP. Finally we have performed atomistic simulations of active-site dynamics based on an on-path "transition-state" myosin conformation, which has revealed significantly weakened coordination of phosphate by Switch II, and a disrupted key salt bridge between Switch I and II. Meanwhile, the coordination of MgADP by Switch I and P loop is less perturbed. As a result, the phosphate can be released prior to MgADP. This study has shed new lights on the controversy over the structural mechanism of actin-activated phosphate release and force generation in myosin motor.

Proteins 2010; 78:638–660.

Key words: myosin; actin; force generation; powerstroke; normal mode analysis; elastic network model; multiscale modeling; allosteric coupling; transition pathway.

INTRODUCTION

Myosins—a superfamily of actin-based motor proteins powered by adenosine triphosphate (ATP) hydrolysis, are involved in a diversity of functions ranging from muscle contraction to intracellular transportation.[1] Among at least 20 myosin classes,[2] Class II myosin (or Myosin II) has been under intensive investigations for decades by biochemical, biophysical, genetic, and structural experiments (see Refs. 3–5). More recently, Class V myosin (or Myosin V)—a dimeric motor that walks along actin filaments processively by alternating its two heads,[6–8] has attracted tremendous interests (see Ref. 9). A central question in myosin function is: how does myosin motor harness the free energy from ATP hydrolysis and/or actin binding to produce mechanical forces and movements? Mounting evidence has outlined a "mechano-chemical coupling" mechanism involving a cascade of nucleotide-dependent conformational changes between a series of biochemical states in actomyosin (see below)—these conformational changes are thought to orchestrate the allosteric couplings among actin binding/release, nucleotide binding/release, and force generation. To understand the structural basis of mechano-chemical coupling in myosin motor, a major challenge is to probe these conformational changes with high spatial and temporal resolutions. Synergetic efforts that combine experimental approaches with computer modeling promise to meet this great challenge.

The primary kinetic cycle of a monomeric actomyosin has been outlined by extensive kinetic studies,[10–12] which consists of at least six biochemical states:

A-M → **A-M-ATP** → **M-ATP** → **M-ADP-Pi** →
A-M-ADP-Pi → **A-M-ADP** → **A-M**

(**A: actin, M**: myosin, **Pi**: γ-phosphate)

Starting from the **A-M** state (or post-powerstroke state), ATP binding dissociates myosin rapidly from actin. ATP hydrolysis leads to **M-ADP-Pi** state (or pre-powerstroke state), which is accompa-

Additional Supporting Information may be found in the online version of this article.
Grant sponsor: American Heart Association; Grant number: 0835292N.
*Correspondence to: Wenjun Zheng; Physics Department, University at Buffalo, Buffalo, NY 14260. E-mail: wjzheng@buffalo.edu.
Received 29 April 2009; Revised 25 July 2009; Accepted 12 August 2009
Published online 27 August 2009 in Wiley InterScience (www.interscience.wiley.com).
DOI: 10.1002/prot.22594

nied by an upward rotation of the lever arm to the pre-powerstroke position (named recovery stroke). Actin binding accelerates Pi release from myosin, resulting in force generation (or powerstroke) as the lever arm rotates downward to the post-powerstroke position (lever arm hypothesis[3–5]). Subsequent release of ADP returns myosin to the **A-M** state for the next cycle. Despite the conservation of ATPase cycle, the kinetic rates vary greatly among myosin isoforms.[13] In fast Myosin II, the actin-activated Pi release (or the transition from weak to strong actin-binding affinity prior to Pi release[14]) is rate-limiting, whereas Myosin V features rate-limiting ADP release.[15] Therefore the kinetic cycle time of fast Myosin II is dominated by weak actin-binding states, while Myosin V spends most of its cycle time in strong actin-binding states.[15] The mechanistic basis of myosin's isoform-dependent kinetics has been under active investigations (see Ref. 16), but remains not fully understood.

Detailed structural information is not available for all biochemical states of actomyosin. High resolution myosin structures bound with various nucleotide analogs were solved for two weak actin-binding states (**M-ATP** and **M-ADP-Pi**[17–21]), and a rigor-like state (similar to **A-M** state) that can bind actin strongly.[22–25] To date, no crystal structure of actomyosin at strong actin-binding states has been solved. Low-resolution actomyosin models were built by docking myosin crystal structure and F-actin model[26] into cryo-electron microscopy (cryo-EM) maps of myosin-decorated actin filaments.[27–32] The docking studies have revealed a closed actin-binding cleft in myosin motor domain.[27,31] Central to the force generation and product release processes in actomyosin are the transient states between the **A-M-ADP-Pi** state and the **A-M** state. These structurally elusive states have been characterized by biochemical experiments[33]—including the Sleep-Hutton state (denoted as **A-M$_{SH}$-ADP$_S$**) following rapid Pi release,[34,35] and two ADP-bound states with strong and weak ADP-binding affinity, respectively (denoted as **A-M-ADP$_S$** and **A-M-ADP$_W$**). The lack of detailed structural information for these transient states (except **A-M-ADP$_W$**[24]) has hindered a lucid understanding of the structural events that couple strong actin binding to the sequential release of Pi and ADP, and the initiation of force generation.

The myosin motor domain consists of four subdomains—Upper and Lower 50-kDa subdomains (denoted as U50 and L50), N-terminal subdomain and converter [see Fig. 1(b)]. The nucleotide-binding site, located at the interface between U50, L50, and N-terminal subdomains, consists of four highly conserved motifs essential for nucleotide binding/hydrolysis—P loop, Switch I, Switch II, and the base [see Fig. 1(a)]. The outer cleft between U50 and L50 subdomains is involved in actin binding.[27] The converter is adjoined to a lever arm which is responsible for force generation via a large swing motion.[3–5] It is widely believed that the above key myosin parts are allosterically coupled via a number of key structural elements—including several flexible joints[21] [such as Switch II, relay helix and SH1 helix, see Fig. 1(b)], and a seven-stranded central β-sheet that spans from U50 to N-terminal subdomain [see Fig. 1(a)].[23–25]

Structural comparisons have revealed two pairs of allosterically coupled structural changes in myosin motor domain in the absence of actin [see Fig. 1(a)]: the first pair is between the closing/opening of Switch II (relative to P loop) and the upward/downward swing motion of converter and lever arm,[3] which is involved in the tight coupling between ATP hydrolysis and the recovery stroke of lever arm[36–39]; the second pair is between the closing/opening of the actin-binding cleft and the opening/closing of Switch I (relative to P loop),[22–25] which underlies the reciprocal coupling between actin binding and nucleotide binding in myosin.[40–43] However, the functional roles of these "structural coupling rules" in the presence of strong actin–myosin interactions remain controversial. In one study based on the analysis of a rigor-like structure of Myosin V, it was found that the downward swing motion of converter and lever arm can proceed via a twisting of the central β-sheet without the opening of Switch II.[32] Several studies found a long-lived ADP-bound state with high binding affinity for both actin and ADP in smooth muscle Myosin II[42] and Myosin V.[15] Therefore, an unknown myosin conformation exists with both actin-binding cleft and nucleotide-binding site closed, as confirmed by recent FRET studies.[44,45]

Structure-based computer modeling has been increasingly employed to complement experimental efforts to elucidate the microscopic basis of myosin motor function. At atomistic resolution, molecular dynamics (MD) simulation, energy minimization, and quantum calculation have been used to explore myosin's active-site dynamics,[38,46] ATP hydrolysis,[47–49] recovery stroke,[37–39,50–53] and the actin–myosin interactions.[54] Nevertheless, the very long time scale of the actomyosin kinetic cycle (up to $\sim 10^{-1}$ s) has hampered extensive MD simulations of conformational changes between the biochemical states of actomyosin. To overcome the time-scale barrier, coarse-grained modeling has been developed using simplified structural representations and energy functions.[55] A prime example of coarse-grained models is the elastic network model (ENM) which represents a protein structure as a network of C_α atoms connected by springs.[56–58] In an ENM, the all-atom force fields are replaced by simple harmonic potentials with a uniform force constant[59] (or two force constants[60] for bonded and nonbonded interactions between residues, see Methods). Early studies have shown that the collective motions predicted by the normal mode analysis (NMA) of ENM are insensitive to the dramatic simplification in ENM.[56–58] The low-frequency modes calculated from

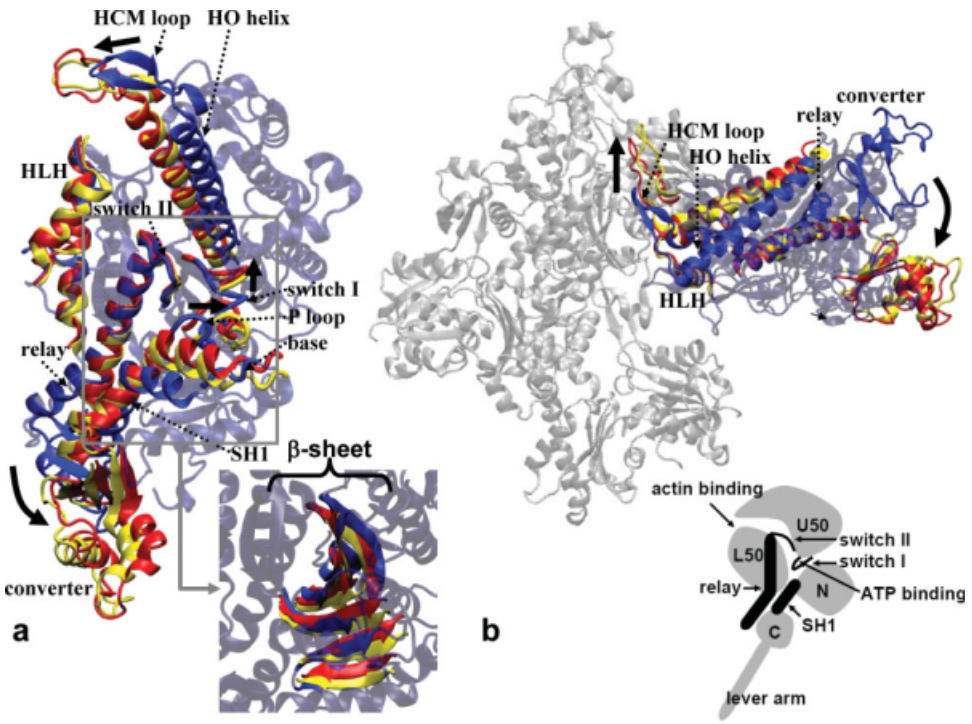

Figure 1

Structural models of actomyosin at the pre-powerstroke and post-powerstroke states: (**a**) front view of myosin motor domain. (**b**) Side view of the entire actomyosin. The lower inset of panel (a) shows the central β-sheet. The lower inset of panel (b) shows the four myosin subdomains—Upper and Lower 50 kDa (U50 and L50), N-terminal (N) and Converter (C), which are connected by several flexible joints (relay helix, SH1 helix and Switch II). Three actomyosin models are shown—one at **A-M-ADP-Pi** state (modeled from the PDB structure 1VOM, colored blue), two at **A-M** state (modeled from the PDB structures 1OE9 and 2OVK, colored red and yellow). The two **A-M** state models are only partially shown for clarity. Three actin subunits are colored gray in panel (b). Key structural elements in all three models are shown as opaque cartoons and labeled, whose movements from **A-M-ADP-Pi** state to **A-M** state are shown by thick arrows. The structural changes shown here are only a highlight of all observed changes from previous structural studies (for more details, see Refs. 22–25).

ENM were found to compare well with many crystallographically observed structural changes.[58,59,61] Numerous studies have established ENM as an efficient means to probe the conformational dynamics in biomolecular structures with virtually no limit in timescale or system size (see Refs. 62,63). The deformability of ENM allows a more realistic description of structural changes in myosin motor domain than rigid-body motions of subdomains (particularly in the central β-sheet and flexible joints). Recently, the NMA based on ENM or all-atom force fields has been employed to study myosin's global motions,[64,65] local motion at the nucleotide-binding site and its coupling with global motions,[66] dynamic couplings,[39,67] structural flexibility,[42,68] conformational transition pathway,[69] and ATP-binding-induced dissociation from actin.[70] A recent study investigated the structural relaxation of myosin motor domain from the pre-powerstroke state to the near-rigor state using a coarse-grained Gō-like model.[71] These extensive studies have demonstrated the usefulness of NMA and coarse-grained modeling in probing myosin's conformational dynamics. In particular, the low-frequency modes of ENM were found to capture key functional motions in myosin—including a large swing motion of the converter during the powerstroke, and a rotation of the U50 subdomain that accounts for the negative coupling between actin binding and nucleotide binding.[67] The key residues involved in the functional motions[72] and the dynamic couplings[67] in myosin were either validated by mutational studies or found to be highly conserved by sequence analysis.[72]

In this study, we will investigate how actin–myosin interactions regulate the conformational dynamics of myosin motor domain. To this end, we will extend the coarse-grained modeling of an isolated myosin[66,67,69,72] to a multiscale modeling of the entire actomyosin complex [consisting of a *Dictyostelium* Myosin II motor domain bound with three actin subunits, see Fig. 1(b)]. *Dictyostelium* Myosin II is chosen as our model system because it has been widely used for structure–function analysis of myosin motor.[73,74] The unique contribution of this study is its novel combination of coarse-grained modeling of global conformational changes with atomistic simulations of active-site dynamics. We will investigate, with a residue level of detail, how structural changes associated with actin binding couple to distant structural changes associated with product release and force genera-

tion, both near the equilibrium states (**A-M-ADP-Pi** state and **A-M** state) and along the transition pathway between these two states. Then, to understand the structural basis of sequential release of Pi and ADP, we will use atomistic MD simulations to explore how the coordination of Pi and MgADP is differentially weakened at a "transition state" along the predicted transition pathway.

To probe allosteric couplings involved in myosin motor function, we will employ a normal-mode-based correlation analysis[75,76] to investigate how the structural motions of key myosin parts (including the actin-binding cleft, the nucleotide-binding motifs, the central β-sheet, the relay helix, and the converter) are coupled near **A-M-ADP-Pi** state and **A-M** state. At **A-M-ADP-Pi** state, we have pinpointed the following actin-activated couplings to product release and force generation:

1. Actin binding is strongly coupled to a shift between Switch I and II that disrupts their coordination of Pi, and less strongly to the opening of Switch I that weakens the binding of MgADP.
2. Actin binding is strongly coupled to the twisting of central β-sheet which is subsequently coupled to the opening of Switch II.
3. Actin binding is strongly coupled to the unbending of relay helix and the forward movement of converter in the direction of powerstroke, which allows actin binding to directly drive force generation.

By modeling **A-M** state using the rigor-like structures of both Myosin II and V, we have identified the following isoform-dependent couplings which underlie the reciprocal coupling between actin binding and nucleotide binding,[40–43] and the load-dependent ADP release in Myosin V[77–79]:

1. The opening of actin-binding cleft is coupled weakly (strongly) to the closing of Switch I in Myosin V (Myosin II), which explains weak (strong) reciprocal coupling in Myosin V (Myosin II).
2. The backward movement of converter (relative to actin) is strongly (weakly) coupled to the closing of Switch I in Myosin V (Myosin II), which accounts for load-dependent ADP release in Myosin V but not in Myosin II.

To uncover the sequence of structural events underlying force generation and product release in actomyosin, we will perform coarse-grained modeling[69] of the transition pathway (consisting of a series of intermediate structures) from **A-M-ADP-Pi** state to **A-M** state. The intermediate structures along the pathway offer a detailed view to those highly elusive transient states (such as **A-M$_{SH}$-ADP$_S$** state and **A-M-ADP$_S$** state). On the basis of the transition pathway modeling, we have predicted the order of structural events following actin binding that leads to force generation and the sequential release of Pi followed by MgADP. We have found that the force-generating movements (relay helix unbending and converter rotation) start immediately upon actin binding, which are followed by the twisting of central β-sheet, and later the opening of nucleotide-binding site. The predicted order of structural changes qualitatively agrees with the observed structural variations among myosin crystal structures, and the finding of an intermediate state with both actin-binding cleft and nucleotide-binding site closed by recent FRET studies.[44,45] Our finding supports the proposals that force generation occurs before the opening of nucleotide-binding site that allows product release,[80–82] and the central β-sheet is involved in actin-activated force generation and product release.[24]

Finally, to yield atomistic pictures of actin-activated Pi release in actomyosin, we will refine the coarse-grained transition-state myosin model with atomic details, and then perform MD simulations of the active-site dynamics. We will assess how the coordination of Pi and Mg^{2+} by active-site residues is weakened following actin-activated global conformational changes. Along a similar line, a previous simulation found the interaction between Mg^{2+} and Switch I to be weakened following a change in the relay helix and converter conformation during the recovery stroke.[38] We have found significant weakening of the hydrogen bonds between Pi and Switch I and II (particularly Switch II), while the coordination of Mg^{2+} by Switch I and P loop is less perturbed. Additionally, the critical salt bridge between Switch I and II (R238-E459) is temporarily broken, which opens a "backdoor" between Switch I and II to allow Pi release, while MgADP remains bound.

METHODS

Elastic network model

In an ENM, a protein structure is represented as a network of beads each corresponding to the C_α atom of an amino acid residue. A harmonic potential accounts for the elastic interaction between a pair of C_α atoms that are within a cutoff distance R_c = 10Å (alternative R_c = 8, 9, 11, 12Å are tested, which yield similar results of correlation analysis and transition pathway modeling). The ENM potential energy is

$$E = \frac{1}{2}\sum_{i=1}^{N}\sum_{j=1}^{i-1} k_{ij}\theta\left(R_c - d_{ij}^0\right)\left(d_{ij} - d_{ij}^0\right)^2, \qquad (1)$$

where N is the number of C_α atoms, $\theta(x)$ is the Heaviside function, d_{ij} is the distance between the C_α atom i and j, d_{ij}^0 is the value of d_{ij} as given by an equilibrium structure with minimal ENM potential energy. k_{ij} is the force constant which is 1 for nonbonded interactions and

100 for bonded interactions between residues (the unit of k_{ij} can be arbitrarily chosen without changing the modeling results in this study). The use of high/low force constant for bonded/nonbonded pairs of C_α atoms was found to improve the accuracy of ENM-based modeling.[60]

We expand the ENM potential energy to second order:

$$E \approx \frac{1}{2} X^T H X, \tag{2}$$

where X is a $3N$-dimension vector representing the 3D displacement of N C_α atoms away from their equilibrium positions, H is the Hessian matrix which is obtained by calculating the second derivatives of ENM potential energy with respect to the 3D coordinates of C_α atoms.

A normal mode analysis of the Hessian matrix yields $3N$-6 nonzero normal modes (excluding 6 zero modes corresponding to 3 rotations and 3 translations), which are numbered from 1 to $3N$-6 in order of ascending eigenvalue.

To validate ENM, a comparison with the observed structural changes between two experimental structures (represented by a $3N$-dimension vector X_{obs}) is done by calculating the following "per-mode" overlap for the eigenvector W_m of mode m:

$$I_m = \frac{X_{\text{obs}}^T W_m}{|X_{\text{obs}}| \times |W_m|}, \tag{3}$$

where $X_{\text{obs}}^{\text{T}} W_m$ is the dot product between X_{obs} and W_{m}, $|X_{\text{obs}}|$ and $|W_m|$ represent their magnitudes.

In addition, the following cumulative overlap is calculated to assess how well the lowest M modes describe X_{obs}:

$$C_M = \sqrt{\sum_{1 \le m \le M} I_m^2}. \tag{4}$$

Because $\sum_{1 \le m \le 3N-6} I_m^2 = 1, C_M^2$ gives the percentage of the observed structural changes captured by the lowest M modes.

Correlation analysis of the coupling between motions of two protein parts

We have recently developed a correlation analysis to quantify the coupling between the given movements of two parts (named S_1 and S_2) of a protein structure.[76] The crystallographically observed movement of S_1 (S_2) away from an equilibrium structure is represented by a $3N_1$ ($3N_2$) -dimension vector X_1 (X_2), where N_1 (N_2) is the number of residues in S_1 (S_2). X_1 (X_2) can be obtained by structural superposition in the following two ways:

i. To describe the internal movement of S_1 (S_2) (excluding global translations or rotations of S_1 or S_2), $X_1 = X_{1,\text{obs}}$ ($X_2 = X_{2,\text{obs}}$) is obtained by structurally superimposing a target structure on the equilibrium structure along the C_α atoms of S_1 (S_2) with minimal root mean squared deviation (RMSD), and then calculating the 3D displacements of S_1 (S_2) residues from the equilibrium structure to the target structure. For example, the opening/closing of actin-binding cleft in myosin can be obtained in this way.
ii. To describe the global movement (translations and rotations) of S_1 (S_2) relative to another fixed part of protein (named S_{ref}), $X_1 = X_{1,\text{obs}}$ ($X_2 = X_{2,\text{obs}}$) is obtained by structurally superimposing a target structure on the equilibrium structure along the C_α atoms of S_{ref} with minimal RMSD, and then calculating the 3D displacements of S_1 (S_2) residues from the equilibrium structure to the target structure. For example, the movement of converter relative to actin in actomyosin can be obtained in this way, where S_{ref} is chosen to be the actin subunits.

The raw correlation between the observed movements of S_1 (X_1) and S_2 (X_2) away from the equilibrium structure is calculated by summing up weighted contributions from ENM modes as follows:

$$C_{12} = \frac{X_1^T P_1 H^{-1} P_2^T X_2}{|X_1||X_2|} = \sum\nolimits_{1 \le m \le M} \frac{X_1^T P_1 W_m (P_2 W_m)^T X_2}{\lambda_m |X_1||X_2|}, \tag{5}$$

where $H^{-1} = \sum_{1 \le m \le M} \frac{W_m W_m^T}{\lambda_m}$, M is the cutoff mode (M = 3N-6 by default), W_m and λ_m are the eigenvector and eigenvalue of mode m (W_m is normalized to unit magnitude), $P_1(P_2)$ is the projection operator from the 3N-dimension conformational space to the $3N_1$ ($3N_2$)-dimension subspace for S_1 (S_2).

To determine if the raw correlation given in Eq. (5) is statistically significant, the following Z-score analysis is conducted.

We analyze the distribution of C_{12} for randomly assigned $X_1 = X_{1,\text{rand}}$ and $X_2 = X_{2,\text{rand}}$. Singular value decomposition (SVD) gives

$$P_1 H^{-1} P_2^T = U_1 S V_2^T = [u_{11} \quad u_{12} \quad \ldots] \begin{bmatrix} s_1 & 0 & 0 \\ 0 & s_2 & 0 \\ 0 & 0 & \ldots \end{bmatrix} \begin{bmatrix} v_{21}^T \\ v_{22}^T \\ \ldots \end{bmatrix}, \tag{6}$$

where $U_1 = [u_{11}\ u_{12} \ldots]$ ($V_2 = [v_{21}\ v_{22} \ldots]$) is an orthogonal set of $3N_1$ ($3N_2$)-dimension unit vectors, $s_1 \ge s_2 \ldots s_{N_{\text{min}}} \ge 0$, and $N_{\text{min}} = \min(3N_1, 3N_2)$.

Then the correlation between $X_1 = X_{1,\text{rand}}$ and $X_2 = X_{2,\text{rand}}$ is

$$C_{12,\text{rand}} = \frac{X_{1,\text{rand}}^T P_1 H^{-1} P_2^T X_{2,\text{rand}}}{|X_{1,\text{rand}}||X_{2,\text{rand}}|} = \frac{\sum_{1\le m\le N_{\min}} \left(X_{1,\text{rand}}^T u_{1m}\right)\left(v_{2m}^T X_{2,\text{rand}}\right) s_m}{|X_{1,\text{rand}}||X_{2,\text{rand}}|}. \quad (7)$$

After projecting $X_1 = X_{1,\text{rand}}$, $X_2 = X_{2,\text{rand}}$ along the orthogonal vectors from SVD,

$$X_{1,\text{rand}} = \sum_{1\le m\le 3N_1} R_{1m} u_{1m}, \quad X_{2,\text{rand}} = \sum_{1\le m\le 3N_2} R_{2m} v_{2m}, \quad (8)$$

where R_{1m} (R_{2m}) are random numbers with average $\langle R_{1m}\rangle = \langle R_{2m}\rangle = 0$, and variation $\langle R_{1m}^2\rangle = \langle R_{2m}^2\rangle = 1$. Then the variation of $C_{12,\text{rand}}$ is

$$\sigma_C^2 = \left\langle C_{12,\text{rand}}^2 \right\rangle = \left\langle \frac{\sum_{1\le m\le N_{\min}} s_m^2 (R_{1m}R_{2m})^2}{\sum_{1\le m\le 3N_1} R_{1m}^2 \sum_{1\le m\le 3N_2} R_{2m}^2} \right\rangle \sim \frac{\sum_{1\le m\le N_{\min}} s_m^2}{3N_1 \times 3N_2}. \quad (9)$$

The raw correlation C_{12} is rescaled to define the following Z score

$$Z = C_{12}/\sigma_C, \quad (10)$$

which indicates the significance of the computed correlation relative to random fluctuations. A large positive (negative) C_{12} means that the two movements (X_1 and X_2) are correlated (anti-correlated), whereas a small $|C_{12}|$ means that the two movements are not significantly coupled.

Similarly, we can project $X_1 = X_{1,\text{obs}}$, and $X_2 = X_{2,\text{obs}}$ along the orthogonal vectors from SVD:

$$X_{1,\text{obs}} = \sum_{1\le m\le 3N_1} O_{1m} u_{1m}, \quad X_{2,\text{obs}} = \sum_{1\le m\le 3N_2} O_{2m} v_{2m}. \quad (11)$$

Then

$$C_{12} = \frac{\sum_{1\le m\le N_{\min}} s_m O_{1m} O_{2m}}{\sqrt{\sum_{1\le m\le 3N_1} O_{1m}^2 \sum_{1\le m\le 3N_2} O_{2m}^2}}. \quad (12)$$

We can normalize C_{12} by computing the following weighted cross-correlation between the projection coefficients (O_{1m}, O_{2m}):

$$\bar{C}_{12} = \frac{\sum_{1\le m\le N_{\min}} s_m O_{1m} O_{2m}}{\sqrt{\sum_{1\le m\le N_{\min}} s_m O_{1m}^2 \sum_{1\le m\le N_{\min}} s_m O_{2m}^2}}. \quad (13)$$

$\bar{C}_{12}$ ranges from -1 to 1. A value close to ± 1 (say $\bar{C}_{12} > 0.5$) indicates a strong correlation while a value close to zero indicates weak or no correlation.

By properly accounting for the contributions from all ENM modes, the correlation analysis provides an objective evaluation of the net contributions of collective motions to a specific correlation, which is more reliable than the analysis of correlated motions using individual modes.[83]

Perturbation analysis to identify key residues involved in allosteric coupling

To identify the key residues involved in a given correlation [see Eq. (5)], we introduce a residue-position-specific perturbation to the force constant of springs that connect a given residue position i to its neighbors.[84] This perturbation results in the following change to the Hessian matrix:

$$\delta H_i = \sum_{j\ne i} \delta k_{ij} \theta\left(R_c - d_{ij}^0\right) H_{ij}, \quad (14)$$

where H_{ij} is the contribution to Hessian matrix from the elastic interaction between residues i and j. $\delta k_{ij} = \pm\delta k$ if residues i and j are not bonded, and $\delta k_{ij} = 0$ otherwise. For simplicity, a small uniform magnitude (δk) is assumed for the change of force constant. The value of δk can be arbitrarily chosen within the range $0 < \delta k \ll 1$ without changing the modeling results (see below).

Then the first-order perturbation theory predicts that the resulting change in the correlation C_{12} (at cutoff mode $M = 3N\text{-}6$) is

$$\delta C_{12,i} = \frac{-\sum_{j\ne i} \delta k_{ij} \theta\left(R_c - d_{ij}^0\right) X_1^T P_1 H^{-1} H_{ij} H^{-1} P_2^T X_2}{|X_1||X_2|}. \quad (15)$$

So

$$\left|\delta C_{12,i}\right| \le \delta k \cdot S_i, \quad (16)$$

where

$$S_i = \frac{\sum_{j\ne i, i\pm 1} \theta\left(R_c - d_{ij}^0\right) \left|X_1^T P_1 H^{-1} H_{ij} H^{-1} P_2^T X_2\right|}{|X_1||X_2|}. \quad (17)$$

Therefore, the importance of residue position i to the correlation C_{12} is assessed by the S_i score. We will sort the residue positions in order of decreasing S_i and keep the top 15% residues as key residues involved in the correlation C_{12}. Here we assume that a small fraction of all residues are involved in the transmission of an allosteric coupling, although the particular choice of 15% is somewhat arbitrary (it is conceivable that the proper cutoff fraction may vary between proteins). Because the distribution of S_i values peaks at zero and decreases monotonously as S_i increases (data not shown), it is not straightforward to unambiguously define a cutoff value of S_i. Given such uncertainty, we caution that the selection of top 15% residues does not guarantee the selected residues are important, or rule out the unselected residues as unimportant. In this study, we only consider 667 residue positions of myosin motor domain, so the choice of top 15% corresponds to the top 100 residues.

Coarse-grained transition pathway modeling

In a previous work,[69] we proposed a coarse-grained method that generates a transition pathway between two known protein structures. The method was based on a mixed-ENM potential $E_{mix} = f(E_1,E_2)$, where E_1 and E_2 are two ENM potentials [see Eq. (1)] whose equilibrium structure is at the beginning state and end state of a transition, respectively. $E_{mix} = f(E_1, E_2)$ satisfies $E_{mix} \approx E_1$ if $E_1 \ll E_2$ and $E_{mix} \approx E_2$ if $E_2 \ll E_1$.[69] The predicted pathway consists of a series of saddle points (SP) (denoted as X_{sp}), which are determined by the following SP equation with a "mixing" parameter λ varying from 1 to 0[69]:

$$\lambda \nabla E_1(X_{sp}) + (1-\lambda)\nabla E_2(X_{sp}) = 0. \qquad (18)$$

In our previous work,[69] an analytical solution to Eq. (18) was obtained following an approximate second order expansion of E_1 and E_2 [see Eq. (2)]. However, this approximation is inaccurate far away from the equilibrium structure. To remove this inaccuracy, we numerically solve the SP from Eq. (18) using the Newton-Raphson algorithm. The transition-state conformation of the pathway is defined as the SP where E_1 and E_2 cross:$E_1(X_{sp}) = E_2(X_{sp})$.

The predicted pathway allows us to determine the order of structural events involving several parts of a protein. For this purpose, the following reaction coordinate is defined for a given part S:

$$RC_S = 0.5\left(1 + \frac{RMSD_{S,1}^2 - RMSD_{S,2}^2}{RMSD_{S,obs}^2}\right), \qquad (19)$$

where $RMSD_{S,1}$ ($RMSD_{S,2}$) is the RMSD between a given intermediate structure and the beginning (end) state in the C_α atoms of part S, and $RMSD_{S,obs}$ is the corresponding RMSD between the beginning state and end state.

Coarse-grained modeling of actomyosin

We build structural models of actomyosin for **A-M-ADP-Pi** state and **A-M** state as follows:

An **A-M** state model of myosin V (named Holmes model) was previously built based on a rigid-body fit of a rigor-like Myosin V structure (PDB: 1OE9) into the cryo-EM map of Myosin II decorated actin.[32] Based on the Holmes model (including Myosin V and three of the five actin subunits from the original Holmes model), a second **A-M** state model of Myosin II is built by superimposing a rigor-like structure of squid myosin (PDB: 2OVK) with the Holmes model along the HLH motif of L50 subdomain (following Ref. 32). The two structures align very well in the HLH motif (with RMSD in 44 C_α atoms $\sim$0.6 Å). By using the above models of Myosin V and squid myosin as templates, homology modeling is done by the Swiss Model Server (http://swissmodel.expasy.org/workspace/) to build two **A-M** state models for *Dictyostelium* Myosin II (residues 81–747). The consideration of two **A-M** state models allows us to identify isoform-dependent structural couplings in Myosin II and V.

An **A-M-ADP-Pi** state model is built by superimposing a pre-powerstroke structure of *Dictyostelium* Myosin II (PDB: 1VOM, residues 81–747) with the Holmes model along the HLH motif of L50 subdomain (following Ref. 32). The two structures align very well in the HLH motif (with RMSD in 44 C_α atoms $\sim$1.0 Å).

We then construct C_α-only ENMs based on the above actomyosin models (after excluding the ligands such as VO_4, ADP, and Mg^{2+} in 1VOM). The lever arm is not modeled, so we can focus on the allosteric couplings within the myosin motor domain.

The construction of actomyosin models using structures of different myosin isoforms is appropriate because the actin–myosin interface is structurally conserved for different myosin isoforms.[27,28] Following Ref. 32 we assume that during the transition from weak to strong actin-binding affinity the HLH-actin contacts form before the closing of U50-L50 cleft. The alternative assumption that the closing of U50-L50 cleft precedes HLH-actin docking would lead to an orientationally disordered actomyosin conformation at **A-M-ADP-Pi** state, which cannot be modeled by ENM because it requires a uniquely defined equilibrium structure. Our **A-M-ADP-Pi** state model corresponds to the A state of the three-state actin-myosin docking model[85] with an intermediate actin-binding affinity, where the stereo-specific hydrophobic interactions form between actin and the L50 subdomain of myosin. This state is different from the strong actin-binding **A-M-ADP-Pi** state proposed in the kinetic scheme of Lymn and Taylor.[10]

All-atom structural refinement of a coarse-grained model of myosin motor domain

We build an all-atom structural model of myosin motor domain from the C_α-only transition-state model generated by transition pathway modeling. The structural refinement procedure is as follows:

i. An all-atom model of myosin motor domain bound with ADP-Pi is built from a *Dictyostelium* Myosin II structure (PDB: 1VOM). The missing residues (1, 205–208, 711, 716–719, 724–730) are modeled by using the MODLOOP server.[86] Hydrogen atom coordinates are built by the HBUILD[87] module of CHARMM program.[88] The phosphate group is modeled as $H_2PO_4^-$ (following Ref. 38). Crystal waters are removed except three lytic waters (following Ref. 38).

ii. The C_α-only transition-state myosin model is used as a target structure to introduce a harmonic restraint energy $\Delta E_{\text{restraint}} = \frac{1}{2} K \cdot \text{RMSD}^2_{\text{target}}$, where K is a force constant that gradually increases from 1 to 10 Kcal/mol/Å^2, $\text{RMSD}_{\text{target}}$ is the RMSD in C_α atoms relative to the transition-state myosin model. Starting from the all-atom structural model bound with ADP-Pi, we perform 10-round energy minimization using CHARMM program[88] (version c35b1r1) and CHARMM22 force field.[89] At round n (n = 1,...10), $K = n$ Kcal/mol/Å^2, we perform 100 steps of restrained energy minimization (with $\Delta E_{\text{restraint}}$ included in potential energy) using the Adopted Basis Newton-Raphson algorithm[90] followed by 100 steps of unrestrained energy minimization using the Steepest Descent algorithm. Finally, with the C_α coordinates fixed, we perform 1000 steps of energy minimization using the Adopted Basis Newton-Raphson algorithm to further refine the structure. The resulting all-atom model is within RMSD = 0.6 Å in C_α coordinates from the target transition-state myosin model.

MD simulation of active-site dynamics in myosin

Two all-atom myosin models (one built from 1VOM, the other refined from the C_α-only transition-state myosin model generated by transition pathway modeling) are partially solvated in a sphere (radius = 30 Å) of pre-equilibrated TIP3 water molecules,[91] which is centered at the P_β atom of ADP (overlapping waters are deleted). The two models contain 1808 and 1819 water molecules, respectively. The water molecules are confined within the 30-Å-sphere by a weak GEO type of restraining potential using the MMFP module of CHARMM (following Ref. 38). The C_α atoms of myosin residues >20 Å away from the P_β atom of ADP are harmonically restrained (force constant = 1 Kcal/mol/Å^2) to maintain the global conformation of myosin. The use of water-sphere solvation of active site instead of water-box solvation of entire protein is appropriate for the MD simulation of active-site dynamics in myosin as used in previous simulation studies.[38,46]

Ten 1-ns-long MD simulations at constant temperature (T = 300K) are performed after 50 ps of heating using CHARMM program[88] (version c35b1r1) and CHARMM22 force field.[89] The SHAKE algorithm[92] is used to fix all bonds involving hydrogen, with a relative geometric tolerance of 10^{-10}. The time step is set to be 1 fs, and the MD trajectories are saved at 1-ps time interval (the initial 100 ps is discarded). An extended electrostatics model[93] is used to describe electrostatic interactions, where groups beyond 12 Å interact as multipoles (following Ref. 38).

On the basis of the MD trajectories, we calculate the average and standard deviation of atomic distances (e.g., between a hydrogen donor and an oxygen acceptor of a hydrogen bond) relevant to the coordination of Pi and Mg^{2+} by active-site residues (including T186 in P loop, S236, S237, and R238 in Switch I, G457, and E459 in Switch II, see Table I). We monitor the coordination of Mg^{2+} instead of ADP because ADP release in actomyosin is thought to work through weakening the coordination of Mg^{2+}.[3]

To assess if the system is equilibrated within the 1-ns-long MD simulations at transition state, we have generated another 10 2-ns-long MD trajectories (with time step of 2 fs). We have found the average distances to be stable between the first 1 ns and the second 1 ns of the trajectories.

Table I
Statistics of Active-Site MD Simulations: Average (avg.) and Standard Deviation (std.) of Selected Atomic Distances for MD Simulations at Pre-powerstroke State and Transition State

Atomic pair		Avg. (std.) of distance (Å) at pre-powerstroke state	Avg. (std.) of distance (Å) at transition state	Change in avg. of distance (Å)
O1 of Pi	HG1 of S236	2.19 (0.27)	2.45 (0.46)	0.26
O4 of Pi	HN of G457	1.92 (0.18)	2.67 (0.75)	0.75
Mg^{2+}	OG of S237	2.52 (0.31)	2.68 (0.61)	0.16
Mg^{2+}	OG1 of T186	2.06 (0.08)	2.08 (0.09)	0.02
HH12 of R238	OE1 of E459	1.71 (0.10)	2.34 (0.89)	0.63
HH22 of R238	OE2 of E459	1.90 (0.05)	2.25 (0.58)	0.54

Also shown are the changes in avg. between the two states.

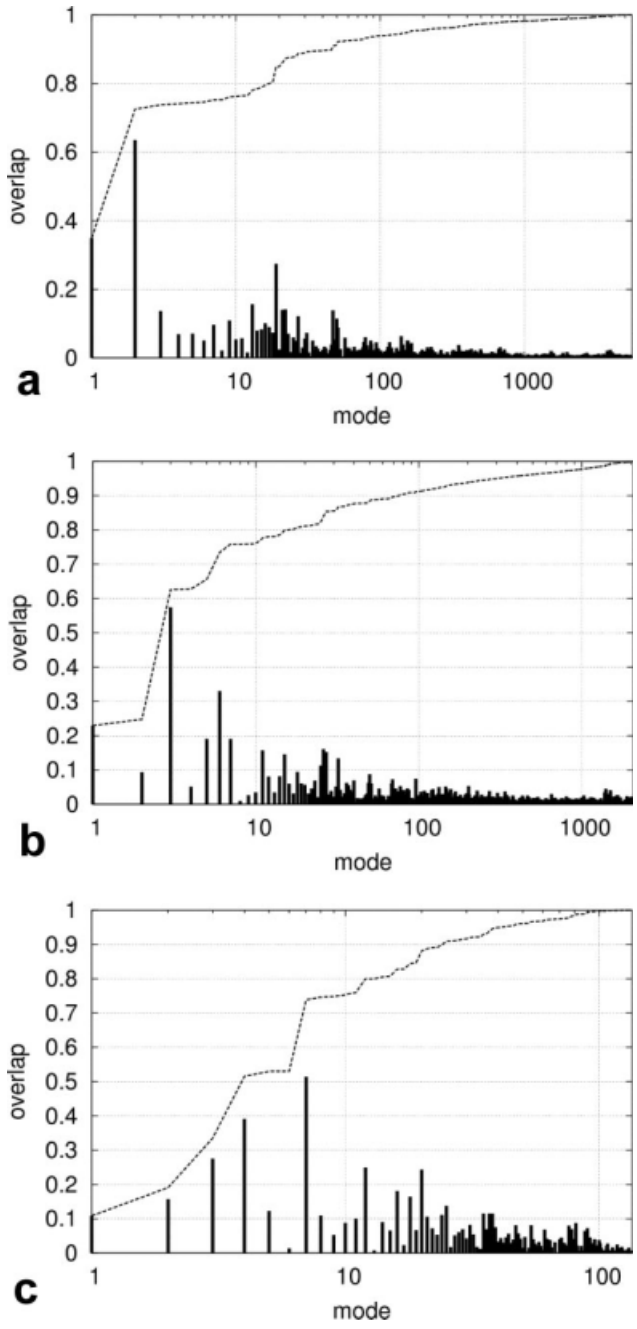

Figure 2

Comparison between the ENM modes and the observed structural changes in: (**a**) the entire actomyosin; (**b**) myosin motor domain (without converter); (**c**) central β-sheet. The per-mode overlaps and cumulative overlaps are shown as impulses and dotted curve, respectively. The per-mode overlap (cumulative overlap) squared gives the percentage of the observed structural changes captured by a given mode (all modes up to a given mode). The mode number is shown in logarithmic scale to offer more clear views of the positions and contributions of low-frequency modes.

RESULTS AND DISCUSSION

Low-frequency ENM modes capture observed conformational changes in actomyosin from A-M-ADP-Pi state to A-M state

Three actomyosin models of *Dictyostelium* Myosin II (one at **A-M-ADP-Pi** state and two at **A-M** state) are built by homology modeling from a cryo-EM-fitted actomyosin model of Myosin V[32] and several crystal structures of Myosin II and V (see Methods).

A structural comparison between the actomyosin models at **A-M-ADP-Pi** state and **A-M** state reveals the following global and local conformational changes (see Fig. 1): a large downward [see Fig. 1(a)] and forward [relative to actin, see Fig. 1(b)] movement of the converter coupled with an unbending of the relay helix, a rotation of the U50 subdomain that closes the actin-binding cleft, a twisting of the central β-sheet[24] [see Fig. 1(a)], and an opening of the nucleotide-binding site. The above structural changes are widely thought to capture the key structural events underlying force generation and product release in myosin motor.[22–24] However the dynamic simulations of these conformational changes are extremely challenging because of their long time scales.

We will validate the ENM by assessing how well the low-frequency ENM modes describe the observed global and local structural changes in actomyosin (see Fig. 1). To describe the global conformational changes in actomyosin, we compute the standard normal modes (named global modes) for the ENM built from the entire actomyosin model at **A-M-ADP-Pi** state. To focus on the local conformational changes within myosin, we calculate the "subsystem" modes[66] for the myosin motor domain (without the converter) or the central β-sheet, while treating the rest of actomyosin as fast-fluctuating "environment."[66] The global (or subsystem) modes are then compared with the observed global (or local) structural changes (see Fig. 1) by calculating the per-mode and cumulative overlaps [see Eqs. (3) and (4) in Methods). Our findings are summarized as follows (see Fig. 2):

1. The observed global conformational changes in actomyosin are dominated by global mode 2 (overlap = 0.64) followed by mode 1 (overlap = 0.35) [see Fig. 2(a)]. The lowest 10 modes (corresponding to <0.2% of total 5583 nonzero modes) capture ∼60% of the observed changes, while the highest contributing mode accounts for ∼41%.
2. The observed conformational changes within myosin motor domain are dominated by low-frequency subsystem modes [see Fig. 2(b)]. The lowest 10 modes (corresponding to <0.5% of total 2067 nonzero modes) capture ∼60% of the observed changes, while the highest contributing mode accounts for ∼32%.

3. The observed twisting of the central β-sheet is collectively described by several low-frequency subsystem modes [see Fig. 2(c)]. The lowest 10 modes (corresponding to ~7% of total 135 nonzero modes) capture ~56% of the observed changes, while the highest contributing mode accounts for ~26%.

Therefore, the low-frequency ENM modes can capture not only large rigid-body movements of myosin's subdomains like converter, but also smaller nonrigid-body motions within myosin motor domain (such as the twisting of central β-sheet). Thus the ENM-based NMA has provided a good framework for modeling the structural dynamics of myosin motor. Notably, we have found that multiple modes are required for an accurate description of the conformational changes within myosin motor domain. Therefore it is important to account for contributions from all low-frequency modes in the modeling of conformational dynamics in actomyosin.[70] Therefore, instead of selecting an arbitrary number of low-frequency modes, we will use a weighted sum of all modes to calculate correlations [see Eq. (5) of Methods]. The transition pathway modeling is based on the solution of a saddle point equation [see Eq. (18) of Methods], which implicitly incorporates contributions from all modes.

Allosterically coupled motions at A-M-ADP-Pi state enable actin binding to trigger product release and force generation

In a previous study, we employed a NMA-based correlation analysis to evaluate how the crystallographically observed motions of various myosin parts couple to each other in a pre-powerstroke myosin structure.[75] That study confirmed the two crystallographically observed couplings—one between the opening of Switch II and the downward rotation of converter,[3] the other between the opening of Switch I and the closing of actin-binding cleft.[23–25] However, it is unclear how actin binding affects these couplings found in detached myosin structures, and whether other unknown structural couplings are enabled in the presence of strong actin binding. To address this critical issue, we will extend the correlation analysis to an actomyosin model at **A-M-ADP-Pi** state, which is built by homology modeling and cryo-EM fitting (see Methods). We will analyze possible couplings that involve the following crystallographically observed structural motions of various myosin parts from **A-M-ADP-Pi** state to **A-M** state (see Fig. 1):

The closing of actin-binding cleft

It is represented by a rotation of the HCM loop of U50 subdomain relative to the HLH motif of L50 subdomain [see Fig. 1(a,b)]—both parts are involved in strong actin binding.[74] The local conformational changes of other actin-binding loops (except HCM loop) are not modeled, partly because they are mostly disordered in myosin crystal structures. Such a simplification in modeling the actin–myosin interface is justified because the ENM-based coarse-grained modeling is insensitive to the local details of actin–myosin interactions, as shown by the robustness of modeling results to the choice of R_c values.

The opening of nucleotide-binding site

It is represented by relative motions between three pairs of nucleotide-binding motifs—(Switch I, P loop), (Switch II, P loop), and (Switch I, II) [see Fig. 1(a)]. The first two motions pertain to the opening of Switch I and II as discussed in previous works (see Ref. 22). The third motion is a lateral shift between Switch I and II, which may perturb the coordination of Pi by Switch I and II.[94] The inclusion of (Switch I, II) shift allows us to characterize local motions that allow Pi release from a closed nucleotide-binding site (see below).

The forward movement of converter

Unlike previous studies that usually describe the rotation of converter with respect to the N-terminal subdomain (see Ref. 75), here it is described relative to actin [see Fig. 1(b)]. This description has two advantages: first, it allows us to explicitly model how the intra-motor-domain motions couple to the movement of myosin relative to actin, which cannot be achieved by modeling myosin motor domain alone[66,67,75]; second, it separates the movement of converter from that of the N-terminal subdomain, and the latter itself undergoes large motions relative to actin [see Fig. 1(a)].

The unbending of relay helix

The relay helix is widely believed to play a key role in coupling the nucleotide-binding site with the rotation of converter and lever arm.[3] During force generation, the transition from bent to straight conformation in relay helix is tightly coupled to the downward rotation of converter and lever arm [see Fig. 1(a,b)].

The twisting of central β-sheet

A transition of the central β-sheet from a high-energy untwisted conformation (at **A-M-ADP-Pi** state) to a low-energy twisted conformation (at **A-M** state) [see Fig. 1(a)] was thought to drive product release and possibly force generation in myosin motor.[24,25]

A correlation analysis will be carried out to evaluate whether the above observed motions are coupled by the

Table II
Results of Correlation Analysis of Allosteric Couplings in Actomyosin

	Two moving myosin parts		Myosin V specific correlation			Myosin II specific correlation		
State	*S1*	*S2*	C_{12}	*Z score*	$\overline{C}_{12}$	C_{12}	*Z score*	$\overline{C}_{12}$
A-M-ADP-Pi	actin-cleft	β-sheet	+0.0576	+38.84	+0.76	+0.0482	+32.49	+0.69
	actin-cleft	(swI, swII)	+0.1072	+22.88	+0.88	+0.1101	+23.51	+0.88
	actin-cleft	(swI, P loop)	+0.0136	+10.82	+0.52	+0.0185	+14.72	+0.64
	actin-cleft	(swII, P loop)	+0.0362	+9.03	+0.45	+0.0039	+0.96	+0.05
	actin-cleft	relay helix	+0.0826	+22.06	+0.75	+0.0842	+22.48	+0.84
	actin-cleft	converter	+3.3526	+38.51	+0.74	+3.8126	+43.79	+0.76
	β-sheet	(swII, P loop)	+0.0097	+5.13	+0.40	+0.0204	+10.77	+0.70
	relay	(swII, P loop)	−0.0030	−0.80	−0.05	−0.0262	−7.02	−0.45
A-M	actin-cleft	(swI, swII)	+0.0579	+17.49	+0.67	+0.0474	+16.53	+0.77
	actin-cleft	(swI,Ploop,base)	−0.0059	−4.21	−0.13	+0.0161	+11.04	+0.36
	converter	(swI, P loop)	+0.3991	+19.06	+0.72	+0.1658	+5.35	+0.25

Raw correlation [C_{12}, see Eq. (5) of Methods], *Z* score [see Eq. (10) of Methods] and normalized correlation [$\overline{C}_{12}$, see Eq. (13) of Methods] are shown for two myosin parts (*S1* and *S2*). The Myosin V specific correlations are calculated using the **A-M** state model built from the rigor-like structure of chicken Myosin V (PDB: 1OE9). The Myosin II specific correlations are calculated using the **A-M** state model built from the rigor-like structure of squid myosin (PDB: 2OVK). Strong correlations (with *Z* score >1, and $\overline{C}_{12}$>0.5) discussed in the text are underlined.

collective motions described by the ENM modes solved from the actomyosin model at **A-M-ADP-Pi** state. This method allows an objective assessment of the net effects of all ENM modes on a given structural coupling, which can not be reliably deduced by inspecting individual modes.[83] By identifying strongly coupled movements at **A-M-ADP-Pi** state, we can predict early-occurring structural events during the transition from **A-M-ADP-Pi** state to **A-M** state, which complements the modeling of transition pathway (see below).

To explore the isoform-dependence of structural couplings, we have modeled two alternative conformational changes from **A-M-ADP-Pi** state to **A-M** state by using two distinct **A-M** state actomyosin models: one is built from a rigor-like structure of Myosin V,[32] the other from a rigor-like structure of Myosin II (see Methods). Therefore, the conformational changes obtained from the former (latter) **A-M** state model are named "Myosin-V specific" ("Myosin-II specific"). For the lack of a pre-power-stroke crystal structure of Myosin V, we will ignore possible structural differences between Myosin II and V at **A-M-ADP-Pi** state.

The results are summarized as follows (see Table II for details):

Coupling between actin binding cleft and nucleotide-binding site: For both myosin-V and Myosin-II specific conformational changes, strong correlations are found between the closing of actin-binding cleft and the shift of (Switch I, II) (*Z* score $\gg$ 1 and $\overline{C}_{12}$ = 0.88, see Table II), while the correlations of actin binding with the opening of (Switch I, P loop) differ between Myosin-V and Myosin-II specific conformational changes (see below).

The correlation between actin binding and the opening of (Switch I, P loop) is positive for both Myosin-V and Myosin-II specific conformational changes ($\overline{C}_{12}$ = 0.52 and 0.64, see Table II), which suggests that actin binding weakens ADP binding in both Myosin V and II (because MgADP is primarily coordinated by Switch I and P loop). Interestingly, this correlation is 36% stronger for Myosin-II specific conformational changes than Myosin-V specific ones (based on a comparison of raw correlation C_{12}, see Table II), which supports a stronger negative coupling between actin binding and ADP binding in Myosin II than Myosin V.[15,41,42]

Actin binding couples more strongly to the shift of (Switch I, II) than the opening of (Switch I, P loop) (see Table II). Because Pi is primarily coordinated by S236 of Switch I and G457 of Switch II,[19,94] while MgADP is primarily coordinated by S237 of Switch I and T186 of P loop, it is likely that these two local motions are separately involved in Pi and MgADP release. Therefore, the above difference in coupling strength may lead to differential perturbations by actin binding to the coordination of Pi and MgADP, which may facilitate a sequential release of Pi followed by MgADP.

Coupling between actin binding cleft and central β-sheet: For both Myosin-V and Myosin-II specific conformational changes, the correlation between the closing of actin-binding cleft and the twisting of central β-sheet is strongly positive (*Z* score $\gg$ 1 and $\overline{C}_{12}$ = 0.76 and 0.69, see Table II), and the latter is positively coupled to the opening of (Switch II, P loop) ($\overline{C}_{12}$ = 0.40 and 0.70, see Table II). Therefore, actin binding can indirectly induce the opening of (Switch II, P loop) via the twisting of central β-sheet, especially in Myosin II where the coupling between actin binding and the opening of (Switch II, P loop) is very weak ($\overline{C}_{12}$ = 0.05, see Table II). This finding substantiates the proposed role of central β-sheet in controlling product release during force generation.[23,24]

Table III
Results of Perturbation Analysis of Key Residues Involved in Two Selected Allosteric Couplings in Actomyosin

Correlation between	Top 15% key residues of myosin
Actin-cleft closing and converter movement at **A-M-ADP-Pi** state	231, 272, 358, 391, 395, 397-400, 402-407, 420, 432, 459-462, 477, 481, 508-511, 514-520, 522-523, 529-530, 533-541, 544, 550, 558-562, 564-570, 572-578, 580-582, 584-589, 591, 593, 595, 597, 620-621, 625-627, 629-630, 632-637, 642, 645-646, 650, 677-678, 680
(switch I, P loop) closing and converter movement at **A-M** state	89-90, 121, 125, 149, 152-155, 158, 176, 178-193, 212, 216, 222, 227-229, 232-242, 263, 276, 315, 453-461, 471-479, 481, 485, 510, 513-514, 517, 521, 561, 570, 572-578, 627, 642, 646, 651, 653-654, 656-657, 660, 674-684

The coordination between actin binding and the twisting of central β-sheet allows concerted release of free energy from both processes to drive product release and force generation in myosin motor.[25]

Coupling between actin binding cleft and relay helix and converter: For both Myosin-V and Myosin-II specific conformational changes, the closing of actin-binding cleft is found to couple strongly to the unbending of relay helix (Z score $\gg 1$ and $\overline{C}_{12} = 0.75$ and 0.84, see Table II) and the forward movement of converter (Z score $\gg 1$ and $\overline{C}_{12} = 0.74$ and 0.76, see Table II). This finding supports a direct coupling from actin binding to force generation that does not involve an intermediate structural change at the nucleotide-binding site such as the opening of Switch II.[22,95] This result agrees with the proposal that the removal of the kink on relay helix can be achieved without the opening of Switch II.[32] Indeed, we have found a negative correlation between the opening of (Switch II, P loop) and the unbending of relay helix ($\overline{C}_{12} = -0.05$ and -0.45, see Table II). The finding of a direct coupling from actin binding to force generation is also consistent with the proposal that the initiation of force generation accompanies the transition from weak to strong actin-binding affinity prior to Pi release.[96–100]

To further identify the key residues involved in the transmission of "long-range" couplings, we introduce residue-position-specific perturbations to the ENM force constant and then calculate how much the correlation changes in response to such perturbations (see Methods). This procedure allows us to predict those key residue positions whose perturbation strongly affects the given correlation.

We have applied the perturbation analysis to the correlation between the closing of actin-binding cleft and the forward movement of converter relative to actin. Many of the predicted key residues (see Table III) are located at the actin–myosin interface (including HCM loop and HLH motif) and within the L50 subdomain [see Fig. 3(a)]. Some are distant from both the actin–myosin interface and the converter, including several at the nucleotide-binding site (T231 near Switch I, E459-K462 in Switch II, *Dictyostelium* myosin II residue numbers, same below), some at the L50-N-terminal interface including the fulcrum of relay helix [F481, L508-Q511, H572-M578, R677-C678, G680, see Fig. 3(a)]. Most of them are highly conserved with ConSurf grade ≥ 8 (the ConSurf grade ranges from 1 to 9 with Grade 9 being the most conserved[101]), including E459, I460, F461, F481, D509, S510, Q511, H572-G575, V577, C678, and G680.

Interestingly, no key residues are found at the interface between the relay loop and converter [see Fig. 3(a)], suggesting that this rigid interface is not involved in the coupling between actin binding and converter movement. This result agrees with the finding that the intensity of fluorescence from W501 (located at the relay loop) is not significantly changed by actin binding.[102]

On the basis of perturbation analysis, we predict that mutations to the above key residues will compromise the coupling between actin binding and force generation, and result in defective motor function. Indeed, the G680V mutation was found to impair the actin-activated Pi release and force generation.[103,104] A hypertrophic-cardiomyopathy-causing mutation (G584R) of the human β-cardiac myosin maps to G575 of *Dictyostelium* myosin II.[73] Mutations to the fulcrum of relay helix (F481A and F482A) were found to reduce actin-binding affinity and the rate of actin-activated ATPase.[105]

In sum, our correlation analysis of allosterically coupled motions at **A-M-ADP-Pi** state has revealed differential couplings between actin binding and the nucleotide-binding site—the closing of actin-binding cleft is coupled strongly to a shift of (Switch I, II), but its coupling to the opening of (Switch I, P loop) is weaker and differs between Myosin II and V. Such differential couplings may allow actin binding to trigger sequential release of Pi followed by ADP in an isoform-dependent manner.[35] In addition, we have found a strong coupling between actin binding and the twisting of central β-sheet, which allows the release of energy stored in the "untwisted" central β-sheet upon actin binding to drive product release and force generation. We have also found a direct coupling from actin binding to the forward movement of converter, which allows the free energy released from actin binding to power the movements of myosin motor.

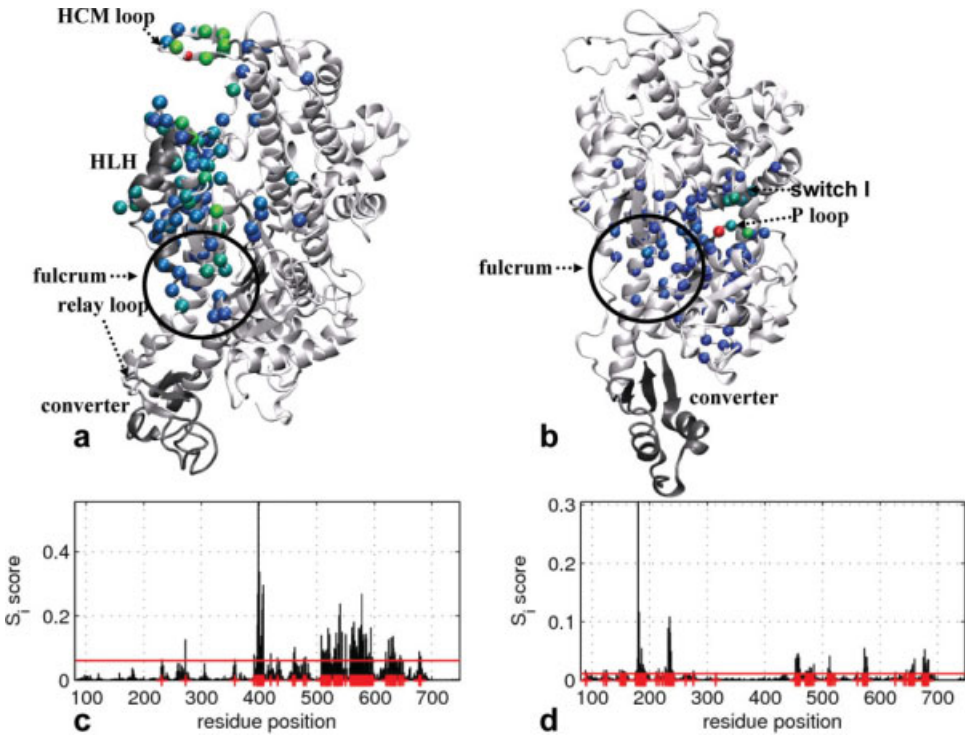

Figure 3

The predicted key residues involved in the following two correlations: (**a**) between the closing of actin-binding cleft and the forward movement of converter at **A-M-ADP-Pi** state; (**b**). between the closing of Switch I (relative to P loop) and the backward movement of converter at **A-M** state. The two myosin parts involved in the correlations are colored gray and the rest of myosin is colored white. The key residues are shown as spheres and colored according to S_i scores (high/medium/low S_i corresponds to red/green/blue color). The structural elements involved in the correlations are labeled. Panels (**c**) and (**d**) show the distributions of S_i scores for the above two correlations. The cutoff S_i for top 15% key residues is shown by a red horizontal line, and the key residue positions are marked by red pluses.

Allosterically coupled motions at A-M state support reciprocal coupling between actin binding and nucleotide binding, and load-dependent ADP release

To explore the allosteric couplings among various myosin parts near the post-powerstroke state, we will apply the correlation analysis to two actomyosin models at **A-M** state, which are constructed using the rigor-like structures of Myosin V and II (see Methods). We will analyze possible couplings that involve the following structural motions in actomyosin from **A-M** state to **A-M-ADP-Pi** state (see Fig. 1):

The opening of actin-binding cleft

It is represented by a rotation of the HCM loop of U50 subdomain relative to the HLH motif of L50 subdomain, which leads to weakened actin-myosin binding.

The closing of nucleotide-binding site

It involves the relative motions of three pairs of nucleotide-binding motifs—closing of (Switch I, P loop) and (Switch II, P loop), and a shift of (Switch I, II). In addition, to describe the local motions at nucleotide-binding site relevant to nucleotide binding, we consider the closing movements of three nucleotide-binding motifs—Switch I, P loop, and base [see Fig. 1(a)]. The relevance of base movement in nucleotide binding is supported by the finding of a large fluorescence quench of W129 (in the base motif) on either ATP or ADP addition.[106]

The backward movement of converter relative to actin

It couples to a backward force applied to the lead head of myosin V dimer by the rear head.

A correlation analysis will be performed to evaluate whether the above motions are coupled by the ENM modes solved from the two actomyosin models at **A-M** state. The consideration of both **A-M** state models of myosin II and myosin V allows us to explore the isoform-dependence in structural couplings.

Coupling between actin-binding cleft and nucleotide-binding site. A reciprocal thermodynamic coupling between actin-binding site and nucleotide-binding site has been well known—either actin or nucleotide, but not

both, can be tightly bound to myosin.[40–43] The strength of reciprocal coupling differs between ADP and ATP in an isoform-dependent manner—ATP binding causes rapid dissociation of myosin from actin; ADP binding couples loosely to actin binding in myosin V[15] and smooth muscle myosin II,[41,42] but strongly in fast myosins such as skeletal and cardiac myosin[41] and *Dictyostelium* myosin II.[43]

For both Myosin V and II, strong correlations are found between the opening of actin-binding cleft and the shift of (Switch I, II) (Z score $\gg 1$ and $\overline{C}_{12} = 0.67$ and 0.77, see Table II), while the correlation of actin unbinding with the closing of (Switch I, P loop, base) differs between Myosin V and II (see below).

The finding of a strongly positive correlation between the opening of actin-binding cleft and the shift of (Switch I, II) allows ATP-induced dissociation of myosin via a Pi-triggered shift between Switch I and II. Indeed, a highly conserved "switching mechanism" is thought to be utilized by myosin, kinesin and G proteins[94] which involves the coordination of Switch I and II in the presence of γ-phosphate. This coupling cannot be triggered by ADP binding for the lack of a γ-phosphate in ADP.

The finding of a weak correlation between the opening of actin-binding cleft and the closing of (Switch I, P loop, base) in myosin V ($\overline{C}_{12} = -0.13$, see Table II) suggests that it can bind MgADP tightly without weakening actin-myosin binding. Therefore myosin V can reach a strong actin-binding and strong ADP-binding state (**A-M-ADP$_S$** state).[15,33] On the contrary, in Myosin II, the finding of a positive correlation between the opening of actin-binding cleft and the closing of (Switch I, P loop, base) ($\overline{C}_{12} = 0.36$, see Table II) implies a stronger reciprocal coupling between actin binding and ADP binding as found in fast myosins.[41,43]

Coupling between nucleotide-binding site and converter. This coupling is relevant to the load-dependent isomerization from **A-M-ADP$_S$** state to **A-M-ADP$_w$** state in myosin V[15,33] (**A-M-ADP$_w$** state is structurally similar to **A-M** state[24]). The load-dependence is attributed to a structural coupling between the isomerization step and a downward rotation of lever arm, as observed in an EM study.[30] This coupling is functionally significant because it enables strain-based coordination of kinetics between two myosin heads which is widely believed to be central to the processive motility of Myosin V.[33]

The correlation between the closing of (Switch I, P loop) and the backward movement of converter (relative to actin) is found to be strongly positive in myosin V ($\overline{C}_{12} = 0.72$, see Table II), but much weaker in Myosin II ($\overline{C}_{12} = 0.25$, see Table II). Therefore, in Myosin V this strong coupling enables a backward force to induce a closed conformation of switch I that allows tight binding of MgADP, which reduces the rate of ADP release as observed in kinetic and mechanical experiments.[77–79] This correlation also explains the observations of lever arm rotation accompanied with ADP release in Myosin V[30] but not in skeletal muscle Myosin II[107] or *Dictyostelium* Myosin II.[43]

To further identify the key residues involved in the transmission of "long-range" coupling between the nucleotide-binding site and the converter, the perturbation analysis is applied to the correlation between the closing of (Switch I, P loop) and the backward movement of converter. Many of the predicted key residues (see Table III) are located near the nucleotide-binding site [see Fig. 3(b)]. Some of them form a path of interacting residues that extends from P loop to the fulcrum region [A183 → I656, I657 → D674-G684, see Fig. 3(b)]. Most of them are highly conserved with ConSurf grade ≥ 8,[101] including A183, I656, Q675, L676, C678, N679, G680, V681, L682, E683, and G684. Based on the perturbation analysis, we predict that mutations to these key residues will compromise the coupling that underlies load-dependent ADP release.

In sum, our correlation analysis of coupled motions at **A-M** state has uncovered the following novel structural couplings in the presence of strong actin binding: the opening of actin-binding cleft is coupled strongly to a shift between Switch I and II, which allows rapid actin-myosin dissociation to be induced by ATP but not ADP; the coupling between the opening of actin-binding cleft and the closing of (Switch I, P loop, base) is positive for Myosin II but not for Myosin V, which allows the formation of a strong actin-binding and strong ADP-binding state in Myosin V but not in Myosin II. In addition, the backward motion of converter relative to actin couples strongly to the closing of (Switch I, P loop) in myosin V but not in Myosin II, which allows a backward force to retard ADP release in myosin V but not in Myosin II.

Coarse-grained modeling of transition pathway reveals a sequence of structural events underlying force generation and product release. The above correlation analysis is limited to small-scale structural motions near the equilibrium states (**A-M-ADP-Pi** state and **A-M** state). To explore large-scale structural changes between the above two equilibrium states, we will perform transition pathway modeling for the transition from **A-M-ADP-Pi** state to **A-M** state. We will construct a smooth pathway consisting of a series of intermediate actomyosin structures with a residue level of details (see Methods).[69] Unlike alternative simulation-based modeling of transition pathways (see Ref. 108), our approach seeks a qualitative prediction of the average features of a structural transition (e.g., the order of structural motions involving various myosin parts) rather than explicit simulations of dynamic trajectories. Our modeling will offer structural insights to those highly elusive transients states

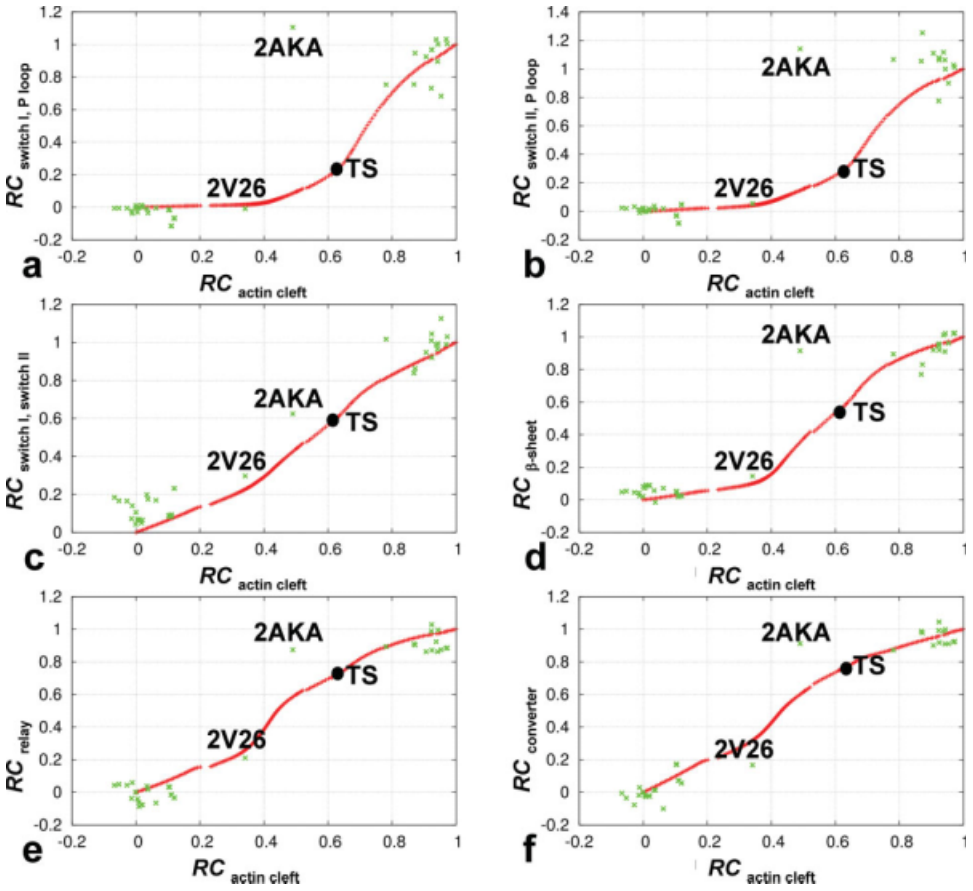

Figure 4

Results of transition pathway modeling for the transition from **A-M-ADP-Pi** state to **A-M** state: Shown here are the 2D projections of the predicted pathway (smooth curve) and myosin crystal structures at pre-powerstroke state and rigor-like state (scattered points). The 2D plane is spanned by the reaction coordinate (*RC*) of the closing of actin-binding cleft [named $RC_{\text{actin cleft}}$, represented by a rotation between the HO helix of U50 subdomain and the HLH motif of L50 subdomain, see Fig. 1(a)] and the *RC* of the following myosin parts: (**a**) (switch I, P loop); (**b**) (switch II, P loop); (**c**) (switch I, switch II); (**d**) central β-sheet; (**e**) relay helix; (**f**) converter (relative to HLH motif) (named $RC_{\text{switch I, P loop}}$, $RC_{\text{switch II, P loop}}$, $RC_{\text{switch I, switch II}}$, $RC_{\beta\text{-sheet}}$, RC_{relay} and $RC_{\text{converter}}$). Most myosin crystal structures at pre-powerstroke state (or rigor-like state) are distributed near (0, 0) (or (1, 1)). Only two myosin structures (PDBs: 2V26 and 2AKA) deviate significantly from the above two states. The predicted transition-state structure (denoted as TS) is also shown, and its associated *RC* values are compared to determine the order of structural events (see text). [Color figure can be viewed in the online issue, which is available at www.interscience.wiley.com.]

involved in the force generation of myosin motor (such as **A-M_{SH}-ADP_S** state and **A-M-ADP_S** state). We note that our modeling is performed on a monomeric acto-myosin in the absence of an external force. It is conceivable that the order of structural motions (particularly the rotation of converter) may change in the presence of an external force or in a myosin dimer with intramolecular strains (see Ref. 109).

To determine the relative order of structural motions, a reaction coordinate (denoted as RC_S) [see Eq. (19) in Methods] is used to quantify the motional progress of a myosin part S (including actin-binding cleft, nucleotide-binding motifs, relay helix, converter and central β-sheet) during a transition. $RC_S = 0$ (1) at the beginning (end) state of the transition from **A-M-ADP-Pi** state to **A-M** state. Along the predicted transition pathway, a transition state is located where the two ENM potentials based at the beginning and end state conformations cross (see Methods). At the transition state [see Fig. 5(a)], a comparison of RC_S between two myosin parts (named S_1 and S_2) determines if S_1 moves earlier (if $RC_{S_1} > RC_{S_2}$) or later (if $RC_{S_1} < RC_{S_2}$) than S_2. Besides the transition state, RC_S is also calculated for the other intermediate structures along the predicted pathway, and multiple myosin crystal structures at pre-powerstroke state (PDBs: 1BR1, 1BR2, 1BR4, 3BZ7, 3BZ8, 3BZ9, 1DFL, 1LKX, 1MND, 1QVI, 2V26, 1VOM, 1W9J, 1W9L, 1YV3) and rigor-like state (PDBs: 2AKA, 2BKH, 2BKI, 2EC6, 2EKV, 2EKW, 1OE9, 2OS8, 2OVK, 1W7I, 1W8J). The crystal structures are used to validate the predicted pathway by

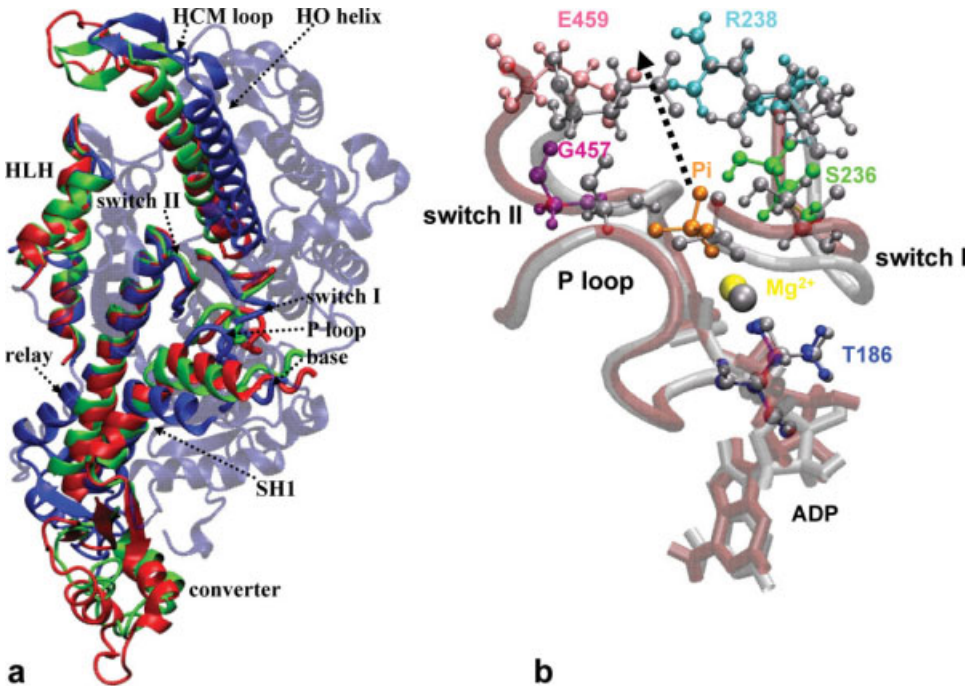

Figure 5

Conformations of myosin motor domain and its active-site at the transition state of the transition from **A-M-ADP-Pi** state to **A-M** state: (**a**) The transition-state myosin model (colored green) is aligned along the HLH motif of L50 subdomain with a myosin model at **A-M-ADP-Pi** state (modeled from the PDB structure 1VOM, colored blue), and a myosin model at **A-M** state (modeled from the PDB structure 1OE9, colored red). The **A-M** state model and transition-state model are only partially shown for clarity. Key structural elements of all three models are shown as opaque cartoons and labeled. (**b**) Two active-site conformations are aligned along P loop—one is from the myosin model at **A-M-ADP-Pi** state (modeled from the PDB structure 1VOM, colored gray), the other is from the end conformation of a 1-ns-long MD simulation starting from the transition-state myosin model (colored red). Key residues involved in the coordination of Pi and Mg^{2+} (T186, S236, R238, G457, E459, except S237) are shown as CPK and colored distinctively. Also shown are the ligands (Pi, Mg^{2+} and ADP). The dotted arrow shows a likely exiting path for Pi after the disruption of the G457-Pi hydrogen bond and the R238-E457 salt bridge.

checking if their distributions overlap in the 2D RC_S plot (see Fig. 4).

At the transition state [see Fig. 5(a)], we have compared RC_S of various myosin parts relative to the closing of actin-binding cleft (the RC_S values correspond to the 2D coordinates of the transition-state conformation in Fig. 4). We have found a clear order of structural events during the transition from **A-M-ADP-Pi** state to **A-M** state:

1. The closing of actin-binding cleft ($RC_{\text{actin cleft}} = 0.63$) is immediately followed by a shift of (Switch I, II) ($RC_{\text{switch I, switch II}} = 0.61$), which is then followed by the opening of Switch II and I relative to P loop ($RC_{\text{switch II, P loop}} = 0.30$, $RC_{\text{switch I, P loop}} = 0.24$) [see Fig. 4(a–c)]. This predicted order agrees with the crystallographic observation of larger structural variations in (Switch I, II) than (Switch I, P loop) and (Switch II, P loop) at the pre-powerstroke state [see Fig. 4(a–c)]. It also agrees with the finding that actin binding couples more strongly with (Switch I, II) shift than the opening of (Switch I, P loop) or (Switch II, P loop) by the correlation analysis (see Table II). Therefore, the closing of actin-binding cleft is not tightly coupled to the opening of Switch I[110] as would have been expected from a rigid-body rotation of U50 subdomain relative to fixed L50 and N-terminal subdomains. Indeed, A FRET study found no change in the energy transfer signal from mant-labeled nucleotide to a FlAsH attached to residues 311-316 of U50 subdomain upon actin-activated Pi release.[44,45] This observation suggests that a closed conformation of Switch I is maintained despite the closing of actin-binding cleft.
2. The closing of actin-binding cleft ($RC_{\text{actin cleft}} = 0.63$) is immediately followed by a twisting of central β-sheet ($RC_{\beta\text{-sheet}} = 0.59$) [see Fig. 4(d)], which agrees with the finding of a strong coupling between actin binding and the twisting of central β-sheet by the correlation analysis (see Table II). Because the twisting of central β-sheet precedes the opening of Switch I or II ($RC_{\beta\text{-sheet}} > RC_{\text{switch II, P loop}}$ and $RC_{\text{switch I, P loop}}$) the former can drive the latter to facilitate product release.

3. The closing of actin-binding cleft ($RC_{\text{actin cleft}} = 0.63$) is accompanied by the unbending of relay helix ($RC_{\text{relay}} = 0.73$) [see Fig. 4(e)] and the downward rotation of converter ($RC_{\text{converter}} = 0.77$) [see Fig. 4(f)], which agrees with the finding of strong couplings between actin binding and the latter two motions by the correlation analysis (see Table II). Together, these results support a direct coupling from actin binding to force generation.

Although most myosin crystal structures are near either **A-M-ADP-Pi** state (at (0, 0) in Fig. 4) or **A-M** state (at (1, 1) in Fig. 4), two of them (PDBs: 2V26 and 2AKA) lie far from the above two states (see Fig. 4), and they may capture intermediate conformations during the transition between the above two states. Indeed, the above predicted order of structural motions is qualitatively captured by 2V26 [the data points of 2V26 lie close to the predicted pathway in Fig. 4(a–f)]. In this structure, the actin-binding cleft is partially closed ($RC_{\text{actin cleft}} = 0.34$), the relay helix is partially unbent ($RC_{\text{relay}} = 0.21$), the converter is partially rotated ($RC_{\text{converter}} = 0.17$), the central β-sheet is partially twisted ($RC_{\beta\text{-sheet}} = 0.15$), Switch I is partially shifted relative to Switch II ($RC_{\text{switch I, switch II}} = 0.30$), while both Switch I and II remain closed ($RC_{\text{switch II, P loop}} = 0.06$, $RC_{\text{switch I, P loop}} = 0$). In comparison, a rigor-like structure of *Dictyostelium* myosin II (PDB: 2AKA) appears to deviate more from the predicted pathway [see Fig. 4(a–f)], suggesting that it may not capture an on-path intermediate during the transition from **A-M-ADP-Pi** state to **A-M** state.

Previous cross-linking and structural studies have found a more flexible conformation of SH1-SH2 helix in the ATP-bound state[111,112] and a more rigid conformation of SH1-SH2 helix in the apo and pre-powerstroke state.[113–115] To study the role of SH1-SH2 flexibility in force generation, we have analyzed transient conformational changes in SH1-SH2 helix along the predicted transition pathway. We have indeed found a transient shortening of SH1 helix by 1 Å during the transition (measured by the distance between the C_α atoms of V681 and K690). The finding of SH1 shortening is robust, which can be obtained using other R_c values between 8 and 12 Å, although the extent of SH1 shortening may be underestimated because ENM does not properly account for plastic deformation or unfolding of a helix. This finding hints for the involvement of a transiently deformed SH1 conformation in force generation. Therefore, the force generation in myosin motor may be inhibited by trapping the deformed SH1 conformation. Indeed, a recent EPR study found that a SH1-SH2-cross-linked actomyosin complex is trapped in an ADP-Pi-bound state during the early stage of force generation.[116] The ability to predict transient structural changes (such as the shortening of SH1 helix), which can not be obtained from a comparison between the pre-powerstroke and rigor-like myosin structures, distinguishes our transition pathway modeling method from alternative methods based on *ad hoc* interpolations between two protein conformations.

Atomistic simulations of active-site dynamics elucidate actin-activated Pi release

Finally, to explore how the global conformational changes induced by actin binding affect the binding of Pi and MgADP, we have conducted ten 1-ns-long MD simulations of the active-site dynamics with explicit solvent (see Methods). The MD simulations start from the refined transition-state myosin model generated by transition pathway modeling (see Methods). As a control, the active-site dynamics at the pre-powerstroke ADP-Pi-bound state is also simulated. We compared the two simulations to explore how the coordination of Pi and Mg^{2+} by active-site residues and the salt bridge between Switch I and II (R238-E459) are weakened at the transition state compared with the pre-powerstroke state. Here we assume the active-site dynamics relevant to Pi and Mg^{2+} coordination is much faster than the global conformational changes along the transition pathway. With the global conformation harmonically restrained (see Methods), both the pre-powerstroke state and transition state behave like an equilibrium state within 1-ns-long MD simulations (see Methods). So we can obtain converged results for the averages and standard deviations of atomic distances based on the MD trajectories. The results are summarized as follows (see Table I, Fig. 6):

1. The hydrogen bonds between Pi and Switch II (Switch I) are strongly (moderately) perturbed at the transition state compared to the pre-powerstroke state [see Fig. 5(b)]. The average distance between the O4 atom of Pi and the HN atom of G457 increases by 0.75 Å [this hydrogen bond is mostly broken during MD simulations at the transition state, see Fig. 6(b)]; the average distance between the O1 atom of Pi and the HG1 atom of S236 increases by 0.26 Å [this hydrogen bond is sometimes broken during MD simulations at the transition state, see Fig. 6(a)]. Therefore, actin binding may facilitate Pi release by weakening the above two Pi-coordinating hydrogen bonds.[19]
2. The electrostatic interaction between Mg^{2+} and Switch I (P loop) is moderately (weakly) perturbed at the transition state compared with the pre-powerstroke state [see Fig. 5(b)]. The average distance between Mg^{2+} and the OG atom of S237 increases by 0.16 Å [this interaction is sometimes broken during MD simulations at the transition state, see Fig. 6(d)], while the average distance between Mg^{2+} and the OG1 atom of T186 is nearly unchanged [see Fig. 6(c)]. Therefore, the coordination of Mg^{2+} is less perturbed

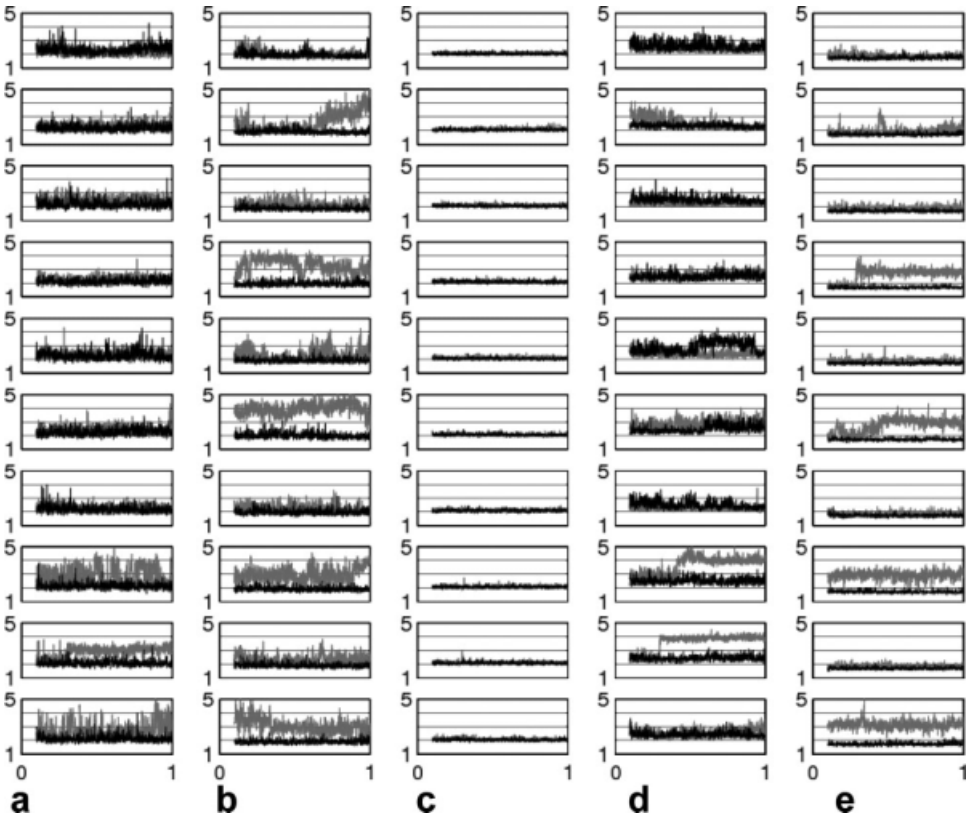

Figure 6

Results of active-site MD simulations that show the following atomic distances (unit Å) as a function of time (unit ns): (**a**) HG1 of S236—O1 of Pi; (**b**) HN of G457—O4 of Pi; (**c**) OG1 of T186—Mg^{2+}; (**d**) OG of S237—Mg^{2+}; (**e**) HH22 of R238—OE2 of E459. Ten 1-ns-long MD trajectories starting from the myosin model at **A-M-ADP-Pi** state (or the transition-state myosin model) are colored black (or gray). Two MD trajectories in each panel start with the same seed for the random number generator used for velocity assignment during the heating stage of MD simulations.

than the coordination of Pi at the transition state, which allows the release of Pi before MgADP.

3. The critical salt bridge between Switch I and II (R238-E459) is significantly perturbed at the transition state compared with the pre-powerstroke state [see Figs. 5(b) and 6(e)]. The average distance between the HH12 (HH22) atom of R238 and the OE1 (OE2) atom of E459 increases by 0.63 Å (0.54 Å). Therefore, the disruption of this key salt bridge may transiently open the Pi-exiting backdoor between Switch I and II[117] at the transition state, although this salt bridge is formed at both **A-M-ADP-Pi** state and **A-M** state. This finding supports the functional role of R238-E479 salt bridge in controlling Pi release besides its catalytic role in ATP hydrolysis as shown by several mutational studies.[118–122]

CONCLUSIONS

In complement with previous simulations of myosin's transitions during the recovery stroke and ATP hydrolysis (**M-ATP → M-ADP-Pi**),[37–39,49–53] and ATP-binding-induced actin-myosin dissociation (**A-M → M-ATP**),[70] the present study focuses on the critical transition (**A-M-ADP-Pi → A-M**) underlying force generation and product release in myosin motor. The conformational dynamics of this transition is not amenable to atomistic MD simulations for its long time scale and the lack of high-resolution structural information for actin–myosin interactions.

By employing a novel combination of multiscale modeling techniques, we have modeled the allosteric couplings and transition pathway of actomyosin with a residue level of details, and the active-site dynamics with atomic details. The NMA-based coarse-grained modeling of actomyosin allows us to make robust predictions for allosteric couplings[75,76] and order of structural events[69] despite the lack of detailed structural information for actin–myosin interactions. The simulation of active-site dynamics based on a transition-state myosin structure allows us to elucidate how the actin-activated global conformational changes perturb the coordination of Pi and MgADP differently to enable their sequential release.

Our coarse-grained modeling of allosteric couplings and transition pathway has revealed a two-stage transition underlying force generation and product release in myosin motor: At the first stage, the closing of actin-binding cleft drives the twisting of central β-sheet [see Table II and Fig. 4(d)], the unbending of relay helix [see Table II and Fig. 4(e)] accompanied by the forward movement of converter relative to actin [see Table II and Fig. 4(f)]. A shift between Switch I and II induced by actin binding [see Table II and Fig. 4(c)] may weaken their coordination of Pi and enable its release, while Switch I is essentially closed [see Table II and Fig. 4(a)] so that MgADP remains bound. At the second stage, the opening of Switch I allows MgADP to release, leading to a further rotation of converter & lever arm in myosin V but not in fast myosin II (see Table II).

The above finding broadly agrees with rich evidence from various experiments (such as optical trapping, FRET, ESR and electron microscopy) of multiple stages during force generation in myosin motor.[36,123–125] The finding that the opening of nucleotide-binding site follows the movements of relay helix and converter is consistent with a simulation study that found the closed state of nucleotide-binding site is energetically stabilized when the converter is in the pre-powerstroke position.[38] The prediction that Pi release occurs from a closed nucleotide-binding site agrees with recent fluorescent studies,[44,45] and an EPR study that found the nucleotide-binding site remains closed at the ADP-Pi-bound state, while it fluctuates between open and closed conformation at the **A-M-ADP$_S$** state.[126] The order by which the actin-binding cleft closes before the nucleotide-binding site opens [see Fig. 4(a,b)] cannot be explained by a rigid-body rotation of the U50 subdomain relative to the rest of myosin motor domain. Instead, highly concerted movements of U50, L50, N-terminal and converter subdomains are required to facilitate direct coupling between actin binding and force generation while maintaining a closed nucleotide-binding site. Our transition pathway modeling will provide guidance to the design of dynamic measurements of these movements using FRET.[44,45]

By analyzing two actomyosin models at **A-M** state constructed from the rigor-like structures of both fast Myosin II and V (see Methods), we have uncovered isoform-dependent allosteric couplings in myosin motor domain. Despite similarities in rigor-like structure between fast Myosin II and V,[25] we have identified allosteric couplings that differ between them. At **A-M** state, the isoform-dependent coupling between actin-binding cleft and Switch I (see Table II) explains why a transient state with high actin-binding and ADP-binding affinities is stabilized in Myosin V but not in fast Myosin II; another isoform-dependent coupling between converter and Switch I (see Table II) explains why ADP release is accompanied by converter rotation in Myosin V but not in fast Myosin II. We attribute the above isoform-dependent couplings to the minor differences in rigor-like structure between fast Myosin II and V,[25] for example in the positions of N-terminal subdomain (including P loop) and converter [see Fig. 1(a)]. Therefore, isoform-dependent tuning of myosin kinetics can be attained by small changes in the relative positions of myosin subdomains in addition to variations in surface loops.[16]

It remains controversial whether Pi is released before or after force generation in myosin motor (see Refs. 33,82). Kinetic studies of myosin ATPase in the absence of actin found that the reversal of recovery stroke occurs before Pi release.[127] The observations of large structural variations in actin-binding cleft and converter at the pre-powerstroke state [see Fig. 4(f)], together with previous experiments on muscle fibers[80,81,128–130] and myosins,[36,131,132] support the scenario that force generation starts before Pi release. However, the finding that Pi release is not significantly changed by intramolecular strains[35] suggests that Pi release occurs before the rotation of converter & lever arm.[102] Our transition pathway modeling, in the absence of an external force, suggests that force generation can be directly triggered by actin binding [see Fig. 4(e,f)] without the opening of nucleotide-binding site [see Fig. 4(a,b)]. This result is consistent with the scenario that Pi release occurs after at least part of the powerstroke, possibly between two working strokes.[133] However, it remains possible that a backward force may alter the transition pathway by retarding the rotation of converter without significantly affecting the movements of Switch I and II related to Pi release. Future simulations will be needed to explore how the presence of an external force affects the transition from **A-M-ADP-Pi** state to **A-M** state.

Previous studies have proposed two competing models for the structural mechanism of Pi release. In a backdoor model, the Pi-exiting pathway opens following the opening of Switch II.[46,117] In an alternative trapdoor model, Pi release is facilitated by the opening of Switch I induced by actin binding.[22,31,134] Our simulations of active-site dynamics have found large actin-activated perturbations to the hydrogen bond between Pi and G457 (in Switch II), and the salt bridge between R238 (in Switch I) and E459 (in Switch II), while the coordination of Mg^{2+} by S237 (in Switch I) and T186 (in P loop) is less affected. The above finding qualitatively agrees with the result of transition pathway modeling ($RC_{\text{switch I, switch II}} > RC_{\text{switch II, P loop}} > RC_{\text{switch I, P loop}}$ at the transition state, see Fig. 4). Although the results of MD simulations of active-site dynamics depend on the accuracy and uniqueness of initial myosin conformations, the above agreement between MD simulations and coarse-grained modeling gives us more confidence in the results of MD simulations. Taken together, we infer that Pi release is facilitated by the actin-activated disruption of Pi coordination by Switch II and the opening of Pi-exiting backdoor locked by the R238-E459 salt bridge, while the coordination of

MgADP by Switch I and P loop remains intact. Our result agrees better with the backdoor model[46,117] than the trapdoor model,[22,31,134] although further MD simulations of more intermediate conformations along the transition pathway may offer more definitive evaluation of the two models.

Our modeling has shed some lights on the energy transduction in actomyosin. Molecular strain in a number of structural elements of the pre-powerstroke myosin conformation, including the untwisted central β-sheet and the bent relay helix,[135] is thought to store the energy from ATP hydrolysis that ultimately powers force generation. Although actin binding contributes zero free energy during the entire myosin work cycle, strong actin binding may still contribute to the loss of free energy needed to perform work.[136] The strong coupling between actin binding and the twisting of central β-sheet allows the concerted release of free energy from both actin binding and ATP hydrolysis to efficiently drive force generation and product release.

ACKNOWLEDGMENTS

The author thanks Dr. Holmes for providing his actomyosin model.

REFERENCES

1. Sellers JR. Myosins: a diverse superfamily. Biochim Biophys Acta 2000;1496:3–22.
2. Berg JS, Powell BC, Cheney RE. A millennial myosin census. Mol Biol Cell 2001;12:780–794.
3. Geeves MA, Holmes KC. Structural mechanism of muscle contraction. Annu Rev Biochem 1999;68:687–728.
4. Spudich JA. The myosin swinging cross-bridge model. Nat Rev Mol Cell Biol 2001;2:387–392.
5. Tyska MJ, Warshaw DM. The myosin power stroke. Cell Motil Cytoskeleton 2002;51:1–15.
6. Mehta A. Myosin learns to walk. J Cell Sci 2001;114 (Part 11): 1981–1998.
7. Forkey JN, Quinlan ME, Shaw MA, Corrie JE, Goldman YE. Three-dimensional structural dynamics of myosin V by single-molecule fluorescence polarization. Nature 2003;422:399–404.
8. Yildiz A, Forkey JN, McKinney SA, Ha T, Goldman YE, Selvin PR. Myosin V walks hand-over-hand: single fluorophore imaging with 1.5-nm localization. Science 2003;300:2061–2065.
9. Sellers JR, Veigel C. Walking with myosin V. Curr Opin Cell Biol 2006;18:68–73.
10. Lymn RW, Taylor EW. Mechanism of adenosine triphosphate hydrolysis by actomyosin. Biochemistry 1971;10:4617–4624.
11. Taylor EW. Mechanism of actomyosin ATPase and the problem of muscle contraction. CRC Crit Rev Biochem 1979;6:103–164.
12. De La Cruz EM, Ostap EM. Relating biochemistry and function in the myosin superfamily. Curr Opin Cell Biol 2004;16:61–67.
13. Marston L, Peacock JL, Calvert SA, Greenough A, Marlow N. Factors affecting vocabulary acquisition at age 2 in children born between 23 and 28 weeks' gestation. Dev Med Child Neurol 2007; 49:591–596.
14. Geeves MA. The dynamics of actin and myosin association and the crossbridge model of muscle contraction. Biochem J 1991;274 (Part 1):1–14.
15. De La Cruz EM, Wells AL, Rosenfeld SS, Ostap EM, Sweeney HL. The kinetic mechanism of myosin V. Proc Natl Acad Sci USA 1999;96:13726–13731.
16. Murphy CT, Spudich JA. Variable surface loops and myosin activity: accessories to a motor. J Muscle Res Cell Motil 2000;21:139–151.
17. Rayment I, Rypniewski WR, Schmidt-Base K, Smith R, Tomchick DR, Benning MM, Winkelmann DA, Wesenberg G, Holden HM. Three-dimensional structure of myosin subfragment-1: a molecular motor. Science 1993;261:50–58.
18. Fisher AJ, Smith CA, Thoden JB, Smith R, Sutoh K, Holden HM, Rayment I. X-ray structures of the myosin motor domain of Dictyostelium discoideum complexed with MgADP. BeFx and MgADP.Al F4. Biochemistry 1995;34:8960–8972.
19. Smith CA, Rayment I. X-ray structure of the magnesium(II).ADP.vanadate complex of the Dictyostelium discoideum myosin motor domain to 1.9 A resolution. Biochemistry 1996; 35:5404–5417.
20. Dominguez R, Freyzon Y, Trybus KM, Cohen C. Crystal structure of a vertebrate smooth muscle myosin motor domain and its complex with the essential light chain: visualization of the pre-power stroke state. Cell 1998;94:559–571.
21. Houdusse A, Szent-Gyorgyi AG, Cohen C. Three conformational states of scallop myosin S1. Proc Natl Acad Sci USA 2000;97: 11238–11243.
22. Reubold TF, Eschenburg S, Becker A, Kull FJ, Manstein DJ. A structural model for actin-induced nucleotide release in myosin. Nat Struct Biol 2003;10:826–830.
23. Coureux PD, Wells AL, Menetrey J, Yengo CM, Morris CA, Sweeney HL, Houdusse A. A structural state of the myosin V motor without bound nucleotide. Nature 2003;425:419–423.
24. Coureux PD, Sweeney HL, Houdusse A. Three myosin V structures delineate essential features of chemo-mechanical transduction. EMBO J 2004;23:4527–4537.
25. Yang Y, Gourinath S, Kovacs M, Nyitray L, Reutzel R, Himmel DM, O'Neall-Hennessey E, Reshetnikova L, Szent-Gyorgyi AG, Brown JH, Cohen C. Rigor-like structures from muscle myosins reveal key mechanical elements in the transduction pathways of this allosteric motor. Structure 2007;15:553–564.
26. Holmes KC, Popp D, Gebhard W, Kabsch W. Atomic model of the actin filament. Nature 1990;347:44–49.
27. Rayment I, Holden HM, Whittaker M, Yohn CB, Lorenz M, Holmes KC, Milligan RA. Structure of the actin-myosin complex and its implications for muscle contraction. Science 1993; 261:58–65.
28. Schroder RR, Manstein DJ, Jahn W, Holden H, Rayment I, Holmes KC, Spudich JA. Three-dimensional atomic model of F-actin decorated with Dictyostelium myosin S1. Nature 1993;364: 171–174.
29. Volkmann N, Hanein D. Actomyosin: law and order in motility. Curr Opin Cell Biol 2000;12:26–34.
30. Volkmann N, Liu H, Hazelwood L, Krementsova EB, Lowey S, Trybus KM, Hanein D. The structural basis of myosin V processive movement as revealed by electron cryomicroscopy. Mol Cell 2005;19:595–605.
31. Holmes KC, Angert I, Kull FJ, Jahn W, Schroder RR. Electron cryo-microscopy shows how strong binding of myosin to actin releases nucleotide. Nature 2003;425:423–427.
32. Holmes KC, Schroder RR, Sweeney HL, Houdusse A. The structure of the rigor complex and its implications for the power stroke. Philos Trans R Soc Lond B Biol Sci 2004;359:1819–1828.
33. Sweeney HL, Houdusse A. The motor mechanism of myosin V: insights for muscle contraction. Philos Trans R Soc Lond B Biol Sci 2004;359:1829–1841.
34. Sleep JA, Hutton RL. Exchange between inorganic phosphate and adenosine 5′-triphosphate in the medium by actomyosin subfragment 1. Biochemistry 1980;19:1276–1283.

35. Rosenfeld SS, Sweeney HL. A model of myosin V processivity. J Biol Chem 2004;279:40100–40111.
36. Shih WM, Gryczynski Z, Lakowicz JR, Spudich JA. A FRET-based sensor reveals large ATP hydrolysis-induced conformational changes and three distinct states of the molecular motor myosin. Cell 2000;102:683–694.
37. Fischer S, Windshugel B, Horak D, Holmes KC, Smith JC. Structural mechanism of the recovery stroke in the myosin molecular motor. Proc Natl Acad Sci USA 2005;102:6873–6878.
38. Yu H, Ma L, Yang Y, Cui Q. Mechanochemical coupling in the myosin motor domain. I. Insights from equilibrium active-site simulations. PLoS Comput Biol 2007;3:e21.
39. Yu H, Ma L, Yang Y, Cui Q. Mechanochemical coupling in the myosin motor domain. II. Analysis of critical residues. PLoS Comput Biol 2007;3:e23.
40. Taylor EW. Kinetic studies on the association and dissociation of myosin subfragment 1 and actin. J Biol Chem 1991;266:294–302.
41. Cremo CR, Geeves MA. Interaction of actin and ADP with the head domain of smooth muscle myosin: implications for strain-dependent ADP release in smooth muscle. Biochemistry 1998;37: 1969–1978.
42. Rosenfeld SS, Xing J, Whitaker M, Cheung HC, Brown F, Wells A, Milligan RA, Sweeney HL. Kinetic and spectroscopic evidence for three actomyosin: ADP states in smooth muscle. J Biol Chem 2000;275:25418–25426.
43. Conibear PB, Bagshaw CR, Fajer PG, Kovacs M, Malnasi-Csizmadia A. Myosin cleft movement and its coupling to actomyosin dissociation. Nat Struct Biol 2003;10:831–835.
44. Sun M, Oakes JL, Ananthanarayanan SK, Hawley KH, Tsien RY, Adams SR, Yengo CM. Dynamics of the upper 50-kDa domain of myosin V examined with fluorescence resonance energy transfer. J Biol Chem 2006;281:5711–5717.
45. Sun M, Rose MB, Ananthanarayanan SK, Jacobs DJ, Yengo CM. Characterization of the pre-force-generation state in the actomyosin cross-bridge cycle. Proc Natl Acad Sci USA 2008;105:8631–8636.
46. Lawson JD, Pate E, Rayment I, Yount RG. Molecular dynamics analysis of structural factors influencing back door pi release in myosin. Biophys J 2004;86:3794–3803.
47. Minehardt TJ, Marzari N, Cooke R, Pate E, Kollman PA, Car R. A classical and ab initio study of the interaction of the myosin triphosphate binding domain with ATP. Biophys J 2002;82:660–675.
48. Schwarzl SM, Smith JC, Fischer S. Insights into the chemomechanical coupling of the myosin motor from simulation of its ATP hydrolysis mechanism. Biochemistry 2006;45:5830–5847.
49. Yang Y, Yu H, Cui Q. Extensive conformational transitions are required to turn on ATP hydrolysis in myosin. J Mol Biol 2008; 381:1407–1420.
50. Woo HJ. Exploration of the conformational space of myosin recovery stroke via molecular dynamics. Biophys Chem 2007;125:127–137.
51. Koppole S, Smith JC, Fischer S. Simulations of the myosin II motor reveal a nucleotide-state sensing element that controls the recovery stroke. J Mol Biol 2006;361:604–616.
52. Koppole S, Smith JC, Fischer S. The structural coupling between ATPase activation and recovery stroke in the myosin II motor. Structure 2007;15:825–837.
53. Mesentean S, Koppole S, Smith JC, Fischer S. The principal motions involved in the coupling mechanism of the recovery stroke of the myosin motor. J Mol Biol 2007;367:591–602.
54. Liu Y, Scolari M, Im W, Woo HJ. Protein-protein interactions in actin-myosin binding and structural effects of R405Q mutation: a molecular dynamics study. Proteins 2006;64:156–166.
55. Tozzini V. Coarse-grained models for proteins. Curr Opin Struct Biol 2005;15:144–150.
56. Atilgan AR, Durell SR, Jernigan RL, Demirel MC, Keskin O, Bahar I. Anisotropy of fluctuation dynamics of proteins with an elastic network model. Biophys J 2001;80:505–515.
57. Hinsen K. Analysis of domain motions by approximate normal mode calculations. Proteins 1998;33:417–429.
58. Tama F, Sanejouand YH. Conformational change of proteins arising from normal mode calculations. Protein Eng 2001;14:1–6.
59. Tirion MM. Large amplitude elastic motions in proteins from a single-parameter. Atomic Analysis Phys Rev Lett 1996;77:1905–1908.
60. Ming D, Wall ME. Allostery in a coarse-grained model of protein dynamics. Phys Rev Lett 2005;95:198103.
61. Krebs WG, Alexandrov V, Wilson CA, Echols N, Yu H, Gerstein M. Normal mode analysis of macromolecular motions in a database framework: developing mode concentration as a useful classifying statistic. Proteins 2002;48:682–695.
62. Bahar I, Rader AJ. Coarse-grained normal mode analysis in structural biology. Curr Opin Struct Biol 2005;15:586–592.
63. Tama F, Brooks CL. Symmetry, form, and shape: guiding principles for robustness in macromolecular machines. Annu Rev Biophys Biomol Struct 2006;35:115–133.
64. Zheng W, Doniach S. A comparative study of motor-protein motions by using a simple elastic-network model. Proc Natl Acad Sci USA 2003;100:13253–13258.
65. Li G, Cui Q. Analysis of functional motions in Brownian molecular machines with an efficient block normal mode approach: myosin-II and Ca2+ -ATPase. Biophys J 2004;86:743–763.
66. Zheng W, Brooks BR. Probing the local dynamics of nucleotide-binding pocket coupled to the global dynamics: myosin versus kinesin. Biophys J 2005;89:167–178.
67. Zheng W, Brooks B. Identification of dynamical correlations within the myosin motor domain by the normal mode analysis of an elastic network model. J Mol Biol 2005;346:745–759.
68. Navizet I, Lavery R, Jernigan RL. Myosin flexibility: structural domains and collective vibrations. Proteins 2004;54:384–393.
69. Zheng W, Brooks BR, Hummer G. Protein conformational transitions explored by mixed elastic network models. Proteins 2007;69: 43–57.
70. Cecchini M, Houdusse A, Karplus M. Allosteric communication in myosin V: from small conformational changes to large directed movements. PLoS Comput Biol 2008;4:e1000129.
71. Takagi F, Kikuchi M. Structural change and nucleotide dissociation of Myosin motor domain: dual go model simulation. Biophys J 2007;93:3820–3827.
72. Zheng W, Brooks BR, Thirumalai D. Low-frequency normal modes that describe allosteric transitions in biological nanomachines are robust to sequence variations. Proc Natl Acad Sci USA 2006;103:7664–7669.
73. Ruppel KM, Spudich JA. Structure-function analysis of the motor domain of myosin. Annu Rev Cell Dev Biol 1996;12:543–573.
74. Sasaki N, Ohkura R, Sutoh K. Dictyostelium myosin II as a model to study the actin-myosin interactions during force generation. J Muscle Res Cell Motil 2002;23:697–702.
75. Zheng W, Thirumalai D. Coupling between normal modes drives protein conformational dynamics: illustrations using allosteric transitions in myosin II. Biophys J 2009;96:2128–2137.
76. Zheng W. Normal-mode-based modeling of allosteric couplings that underlie cyclic conformational transition in F(1) ATPase. Proteins 2009;76:747–62.
77. Rief M, Rock RS, Mehta AD, Mooseker MS, Cheney RE, Spudich JA. Myosin-V stepping kinetics: a molecular model for processivity. Proc Natl Acad Sci USA 2000;97:9482–9486.
78. Veigel C, Wang F, Bartoo ML, Sellers JR, Molloy JE. The gated gait of the processive molecular motor, myosin V. Nat Cell Biol 2002;4:59–65.
79. Purcell TJ, Sweeney HL, Spudich JA. A force-dependent state controls the coordination of processive myosin V. Proc Natl Acad Sci USA 2005;102:13873–13878.
80. Dantzig JA, Goldman YE, Millar NC, Lacktis J, Homsher E. Reversal of the cross-bridge force-generating transition by photogenera-

tion of phosphate in rabbit psoas muscle fibres. J Physiol 1992; 451:247–278.
81. Smith DA, Sleep J. Mechanokinetics of rapid tension recovery in muscle: the myosin working stroke is followed by a slower release of phosphate. Biophys J 2004;87:442–456.
82. Takagi Y, Shuman H, Goldman YE. Coupling between phosphate release and force generation in muscle actomyosin. Philos Trans R Soc Lond B Biol Sci 2004;359:1913–1920.
83. Van Wynsberghe AW, Cui Q. Interpreting correlated motions using normal mode analysis. Structure 2006;14:1647–1653.
84. Zheng W, Brooks BR, Doniach S, Thirumalai D. Network of dynamically important residues in the open/closed transition in polymerases is strongly conserved. Structure 2005;13:565–577.
85. Geeves MA, Conibear PB. The role of three-state docking of myosin S1 with actin in force generation. Biophys J 1995;68(4 Suppl): 194S–199S; discussion 199S–201S.
86. Fiser A, Sali A. ModLoop: automated modeling of loops in protein structures. Bioinformatics 2003;19:2500–2501.
87. Brunger AT, Karplus M. Polar hydrogen positions in proteins: empirical energy placement and neutron diffraction comparison. Proteins 1988;4:148–156.
88. Brooks BR, Bruccoleri RE, Olafson BD, States DJ, Swaminathan S, Karplus M. CHARMM: a program for macromolecular energy, minimization, and dynamics calculations. J Comput Chem 1983;4: 187–217.
89. MacKerell AD, Jr, Bashford D, Bellott M, Dunbrack RL, Jr, Evanseck JD, Field MJ, Fischer S, Gao J, Guo H, Ha S, Joseph-McCarthy D, Kuchnir L, Kuczera K, Lau FTK, Mattos C, Michnick S, Ngo T, Nguyen DT, Prodhom B, Reiher WE, III, Roux B, Schlenkrich M, Smith JC, Stote R, Straub J, Watanabe M, Wiorkiewicz-Kuczera J, Yin D, Karplus M. All-atom empirical potential for molecular modeling and dynamic studies of protein. J Phys Chem B 1998;102:3586–3616.
90. Chu J-W, Trout BL, Brooks BR. A super-linear minimization scheme for the nudged elastic band method. J Chem Phys 2003; 119:12708–12717.
91. Jorgensen WL, Chandrasekhar J, Madura JD, Impey RW, Klein ML. Comparison of simple potential functions for simulating liquid water. J Chem Phys 1983;79:926–935.
92. Ryckaert JP, Ciccotti G, Berendsen HJC. Numerical integration of cartesian equations of motion of a system with constrains—molecular dynamics of *n*-alkanes. J Comput Phys 1977;23:327–341.
93. Steinbach PJ, Brooks BR. New spherical-cutoff methods for long range forces in macromolecular simulation. J Comput Chem 1994; 15:667–683.
94. Vale RD. Switches, latches, and amplifiers: common themes of G proteins and molecular motors. J Cell Biol 1996;135:291–302.
95. Houdusse A, Sweeney HL. Myosin motors: missing structures and hidden springs. Curr Opin Struct Biol 2001;11:182–194.
96. Ostap EM, Barnett VA, Thomas DD. Resolution of three structural states of spin-labeled myosin in contracting muscle. Biophys J 1995;69:177–188.
97. Taylor KA, Schmitz H, Reedy MC, Goldman YE, Franzini-Armstrong C, Sasaki H, Tregear RT, Poole K, Lucaveche C, Edwards RJ, Chen LF, Winkler H, Reedy MK. Tomographic 3D reconstruction of quick-frozen. Ca2+-activated contracting insect flight muscle. Cell 1999;99:421–431.
98. Tsaturyan AK, Bershitsky SY, Burns R, Ferenczi MA. Structural changes in the actin-myosin cross-bridges associated with force generation induced by temperature jump in permeabilized frog muscle fibers. Biophys J 1999;77:354–372.
99. Bershitsky SY, Tsaturyan AK, Bershitskaya ON, Mashanov GI, Brown P, Burns R, Ferenczi MA. Muscle force is generated by myosin heads stereospecifically attached to actin. Nature 1997;388: 186–190.
100. Ferenczi MA, Bershitsky SY, Koubassova N, Siththanandan V, Helsby WI, Panine P, Roessle M, Narayanan T, Tsaturyan AK. The "roll and lock" mechanism of force generation in muscle. Structure 2005;13:131–141.
101. Landau M, Mayrose I, Rosenberg Y, Glaser F, Martz E, Pupko T, Ben-Tal N. ConSurf 2005: the projection of evolutionary conservation scores of residues on protein structures. Nucleic Acids Res 2005;33:W299–W302.
102. Conibear PB, Malnasi-Csizmadia A, Bagshaw CR. The effect of F-actin on the relay helix position of myosin II, as revealed by tryptophan fluorescence, and its implications for mechanochemical coupling. Biochemistry 2004;43:15404–15417.
103. Wu Y, Nejad M, Patterson B. Dictyostelium myosin II G680V suppressors exhibit overlapping spectra of biochemical phenotypes including facilitated phosphate release. Genetics 1999; 153:107–116.
104. Uyeda TQ, Tokuraku K, Kaseda K, Webb MR, Patterson B. Evidence for a novel, strongly bound acto-S1 complex carrying ADP and phosphate stabilized in the G680V mutant of Dictyostelium myosin II. Biochemistry 2002;41:9525–9534.
105. Kintses B, Yang Z, Malnasi-Csizmadia A. Experimental investigation of the seesaw mechanism of the relay region that moves the myosin lever arm. J Biol Chem 2008;283:34121–34128.
106. Kovacs M, Malnasi-Csizmadia A, Woolley RJ, Bagshaw CR. Analysis of nucleotide binding to dictyostelium myosin II motor domains containing a single tryptophan near the active site. J Biol Chem 2002;277:28459–28467.
107. Barsotti RJ, Dantzig JA, Goldman YE. Myosin isoforms show different strokes for different blokes. Nat Struct Biol 1996;3:737–739.
108. Bolhuis PG, Chandler D, Dellago C, Geissler PL. Transition path sampling: throwing ropes over rough mountain passes, in the dark. Annu Rev Phys Chem 2002;53:291–318.
109. Burgess S, Walker M, Wang F, Sellers JR, White HD, Knight PJ, Trinick J. The prepower stroke conformation of myosin V. J Cell Biol 2002;159:983–991.
110. Kintses B, Gyimesi M, Pearson DS, Geeves MA, Zeng W, Bagshaw CR, Malnasi-Csizmadia A. Reversible movement of switch 1 loop of myosin determines actin interaction. EMBO J 2007;26: 265–274.
111. Houdusse A, Kalabokis VN, Himmel D, Szent-Gyorgyi AG, Cohen C. Atomic structure of scallop myosin subfragment S1 complexed with MgADP: a novel conformation of the myosin head. Cell 1999;97:459–470.
112. Himmel DM, Gourinath S, Reshetnikova L, Shen Y, Szent-Gyorgyi AG, Cohen C. Crystallographic findings on the internally uncoupled and near-rigor states of myosin: further insights into the mechanics of the motor. Proc Natl Acad Sci USA 2002;99: 12645–12650.
113. Nitao LK, Reisler E. Probing the conformational states of the SH1-SH2 helix in myosin: a cross-linking approach. Biochemistry 1998;37:16704–16710.
114. Nitao LK, Yeates TO, Reisler E. Conformational dynamics of the SH1-SH2 helix in the transition states of myosin subfragment-1. Biophys J 2002;83:2733–2741.
115. Nitao LK, Loo RR, O'Neall-Hennessey E, Loo JA, Szent-Gyorgyi AG, Reisler E. Conformation and dynamics of the SH1-SH2 helix in scallop myosin. Biochemistry 2003;42:7663–7674.
116. Thompson AR, Naber N, Wilson C, Cooke R, Thomas DD. Structural dynamics of the actomyosin complex probed by a bifunctional spin label that cross-links SH1 and SH2. Biophys J 2008;95: 5238–5246.
117. Yount RG, Lawson D, Rayment I. Is myosin a "back door" enzyme?. Biophys J 1995;68(4 Suppl):44S–47S; discussion 47S–49S.
118. Shimada T, Sasaki N, Ohkura R, Sutoh K. Alanine scanning mutagenesis of the switch I region in the ATPase site of Dictyostelium discoideum myosin II. Biochemistry 1997;36:14037–14043.

119. Sasaki N, Shimada T, Sutoh K. Mutational analysis of the switch II loop of Dictyostelium myosin II. J Biol Chem 1998;273:20334–20340.
120. Li XD, Rhodes TE, Ikebe R, Kambara T, White HD, Ikebe M. Effects of mutations in the gamma-phosphate binding site of myosin on its motor function. J Biol Chem 1998;273:27404–27411.
121. Furch M, Fujita-Becker S, Geeves MA, Holmes KC, Manstein DJ. Role of the salt-bridge between switch-1 and switch-2 of Dictyostelium myosin. J Mol Biol 1999;290:797–809.
122. Friedman AL, Geeves MA, Manstein DJ, Spudich JA. Kinetic characterization of myosin head fragments with long-lived myosin ATP states. Biochemistry 1998;37:9679–9687.
123. Whittaker M, Wilson-Kubalek EM, Smith JE, Faust L, Milligan RA, Sweeney HL. A 35-A movement of smooth muscle myosin on ADP release. Nature 1995;378:748–751.
124. Gollub J, Cremo CR, Cooke R. Phosphorylation regulates the ADP-induced rotation of the light chain domain of smooth muscle myosin. Biochemistry 1999;38:10107–10118.
125. Veigel C, Coluccio LM, Jontes JD, Sparrow JC, Milligan RA, Molloy JE. The motor protein myosin-I produces its working stroke in two steps. Nature 1999;398:530–533.
126. Naber N, Purcell TJ, Pate E, Cooke R. Dynamics of the nucleotide pocket of myosin measured by spin-labeled nucleotides. Biophys J 2007;92:172–184.
127. Malnasi-Csizmadia A, Toth J, Pearson DS, Hetenyi C, Nyitray L, Geeves MA, Bagshaw CR, Kovacs M. Selective perturbation of the myosin recovery stroke by point mutations at the base of the lever arm affects ATP hydrolysis and phosphate release. J Biol Chem 2007;282:17658–17664.
128. Fortune NS, Geeves MA, Ranatunga KW. Tension responses to rapid pressure release in glycerinated rabbit muscle fibers. Proc Natl Acad Sci USA 1991;88:7323–7327.
129. Wang G, Kawai M. Force generation and phosphate release steps in skinned rabbit soleus slow-twitch muscle fibers. Biophys J 1997;73:878–894.
130. Ranatunga KW, Coupland ME, Mutungi G. An asymmetry in the phosphate dependence of tension transients induced by length perturbation in mammalian (rabbit psoas) muscle fibres. J Physiol 2002;542 (Part 3):899–910.
131. Roopnarine O, Szent-Gyorgyi AG, Thomas DD. Microsecond rotational dynamics of spin-labeled myosin regulatory light chain induced by relaxation and contraction of scallop muscle. Biochemistry 1998;37:14428–14436.
132. Agafonov RV, Nesmelov YE, Titus MA, Thomas DD. Muscle and nonmuscle myosins probed by a spin label at equivalent sites in the force-generating domain. Proc Natl Acad Sci USA 2008;105:13397–13402.
133. Smith DA, Geeves MA, Sleep J, Mijailovich SM. Towards a unified theory of muscle contraction. I: foundations. Ann Biomed Eng 2008;36:1624–1640.
134. Pate E, Naber N, Matuska M, Franks-Skiba K, Cooke R. Opening of the myosin nucleotide triphosphate binding domain during the ATPase cycle. Biochemistry 1997;36:12155–12166.
135. Geeves MA, Holmes KC. The molecular mechanism of muscle contraction. Adv Protein Chem 2005;71:161–193.
136. Karatzaferi C, Chinn MK, Cooke R. The force exerted by a muscle cross-bridge depends directly on the strength of the actomyosin bond. Biophys J 2004;87:2532–2544.